

Large eddy simulation of stratified mixing in a two-dimensional dam-break problem in a rectangular enclosed domain

Tamay M. Özgökmen^{a,*}, Traian Iliescu^b, Paul F. Fischer^c,
Ashwanth Srinivasan^a, Jinqiao Duan^d

^a *RSMAS/MPO, University of Miami, Miami, FL, United States*

^b *Department of Mathematics, Virginia Polytechnic Institute and State University, Blacksburg, VA, United States*

^c *Mathematics and Computer Science Division, Argonne National Laboratory, Argonne, IL, United States*

^d *Department of Applied Mathematics, Illinois Institute of Technology, Chicago, IL, United States*

Received 31 October 2005; received in revised form 31 July 2006; accepted 4 August 2006

Available online 28 September 2006

Abstract

Mixing in both coastal and deep ocean emerges as one of the important processes that determines the transport of pollutants, sediments and biological species, as well as the details of the global thermohaline circulation. Both the observations, due to their lack in space and time resolution, and most coastal and general circulation models due to inadequate physics, can only provide partial information about oceanic mixing processes. A new class of nonhydrostatic models supplemented with physically based subgrid-scale (SGS) closures, or so-called large eddy simulation (LES), is put forth as another tool of investigation to complement observational and large-scale modeling efforts.

However, SGS models have been developed primarily for homogeneous, isotropic flows. Here, four SGS models based on Smagorinsky eddy viscosity and diffusivity are tested for stratified flows in the context of 2D dam-break problem in a rectangular enclosed domain. This idealized testbed leads to a number of simplifications about the initial conditions, boundary conditions and geometry, while exhibiting the dynamically complex characteristics of stratified flows involving the interaction of shear-induced mixing and internal waves. Direct numerical simulations (DNS) at high resolutions are taken as benchmark solutions. Under-resolved simulations without SGS terms (so-called DNS^{*}) are used to quantify the impact of SGS stresses. The performance of LES is assessed by using the time evolution of the volume fraction of intermediate density water masses generated by mixing. The simulations are conducted using a nonhydrostatic high-order spectral element model Nek5000 developed to exhibit minimal numerical dissipation and dispersion errors, which is advantageous to quantify accurately the impact of SGS stresses.

It is found that all tested SGS models lead to improved results with respect to those from DNS^{*}. Also, SGS models allow for simulations with coarse resolutions that blow up in DNS^{*} due to lack of adequate dissipation where needed. The SGS model in which the vertical eddy diffusion is modulated via a function that depends on the Richardson number Ri shows the most faithful reproduction of mixed water masses at all resolutions tested.

* Corresponding author.

E-mail address: tozgokmen@rsmas.miami.edu (T.M. Özgökmen).

The sensitivity of the results to the tunable parameter of the SGS model, to changes in the Ri -dependent function and resolution of the turbulent overturning scales is shown.

© 2006 Elsevier Ltd. All rights reserved.

1. Introduction

The large size of the ocean circulation requires decomposition of ocean flows into various scales. At the large scale, ocean flows can be considered to be confined to layers consisting of different density classes, sorted by the effect of stratification, with the flow being approximately two-dimensional (2D) within each layer, due to the Earth's rotation. As scales become smaller and the effects of the Earth's rotation become negligible, fully three-dimensional (3D) flow patterns dominate, which are still influenced by the stratification. 3D stratified fluid motion is enhanced by topographic features such as capes and headlands along the coast (Farmer et al., 2002; Geyer, 1993; Doglioli et al., 2004; Pawlak et al., 2003), sea mounts and ridges at the ocean bottom (Nabatov and Ozmidov, 1988; Gibson et al., 1993; Kunze and Toole, 1997; Lueck and Mudge, 1997; Ledwell et al., 2000; Thurnherr and Speer, 2003; Lavelle et al., 2004) and flows over sills near the straits connecting marginal seas to the oceans (Price and Baringer, 1994). Consequently, these sites are locations of strong vertical mixing, drag and dissipation, and are critical to a successful understanding, numerical simulation and prediction of the ocean circulation. One of the outstanding questions regarding the thermohaline circulation problem is how to generate the vertical diffusivity needed to return back to the surface the dense deep water forming convectively at high latitudes. The vertical mixing processes taking place at these sites can help explain why the effective vertical diffusivity estimated from inverse modeling (Munk and Wunsch, 1998) is an order of magnitude greater than what is measured away from topographic features and boundaries (Kunze and Sanford, 1996). At the small scales, a better understanding of stratified mixing can benefit to problems such as the transport and dispersion of sediments, biological species and pollutants.

Stratified mixing is a challenging problem from the perspectives of both dynamics and numerical modeling. Stratified flows exhibit regimes of shear-induced mixing and internal waves, which are dynamically complex phenomena. The diffusivities of the active tracers (temperature and salinity) are much smaller than viscosity, demanding higher resolution. Also, most ocean models are based on the hydrostatic approximation. The hydrostatic approximation is based on the assumption that the aspect ratio between vertical and horizontal scales is small (cf. Gill, 1982, p. 259). In these cases, the vertical acceleration and dynamic pressure are negligible relative to the horizontal acceleration and hydrostatic pressure. The hydrostatic approximation is adequate for large-scale ocean processes, but it is expected to break down for scales of the order of a few kilometers (Kantha and Clayson, 2000). For internal wave dynamics, the limits of applicability of the hydrostatic approximation are even more restrictive. Inclusion of vertical acceleration and nonhydrostatic pressure is necessary to properly model the evolution of internal waves (Long, 1972). Horn et al. (2001) showed that an initially low frequency, long wavelength internal wave may degenerate into a train of high frequency, short wavelength waves by nonlinear steepening. These solitary waves are short lived, shoaling and breaking at the sloping boundaries, transferring most of larger scale energy to turbulence in the benthic boundary layer (Boegman et al., 2003). During the internal wave propagation, a balance between dynamic pressure and vertical advection holds. Advection is responsible for nonlinear wave steepening and dynamic pressure moderates the steepening rate and disperses the propagating wave into the series of solitary waves. When nonhydrostatic pressure is not modeled while nonlinearities are (i.e. in a hydrostatic model), the wave steepens unabated and may cause an artificial mixing event, depending on the turbulence closures employed. Also, the dispersion relations for internal waves differ in hydrostatic and nonhydrostatic cases. Thus, hydrostatic models not only are not able to correctly represent the shape of the internal waves and their degeneration into solitary waves, but they can also fail to represent the wave-induced boundary mixing. Bourgault and Kelly (2003) show that the mixing due to internal waves is an order of magnitude greater than values predicted by a 3D hydrostatic circulation model. In conclusion, hydrostatic models cannot be used to investigate with accuracy problems involving stratified mixing, and the use of nonhydrostatic models appears to be essential.

Nonhydrostatic modeling can be partitioned into three broad categories. (i) Direct numerical simulation (DNS): in this approach, all scales of motion of a turbulent flow are computed. A DNS must include everything from the large energy-containing scale to dissipative scale. For turbulent flows, DNS requires a large number of grid points (or modes). (ii) Reynolds-averaged Navier–Stokes (RANS): in this approach, all turbulence is modeled (Wilcox, 1998; Safman and Wilcox, 1974; Lam and Bremhorst, 1981; Spalart and Almaras, 1994; Scotti and Piomelli, 2002), but given the complexity of turbulent flows, these models have not been entirely satisfactory. (iii) Large eddy simulation (LES): in this approach, the largest eddies are computed, and the effect of the smaller eddies on the flow is represented by using sub-grid scale (SGS) models. The main underlying concept is the striking feature of a turbulent flow field that, while large eddies migrate across the flow, they carry smaller-scale disturbances with them. Large eddies carry most of the Reynolds stress, and can be different in different types of flows, and thus must be computed, while smaller eddies contribute much less to Reynolds stresses, and may possess a relatively more universal character. The fundamental idea is to compute the large eddies, which carry out most of the mixing, and to model smaller eddies, which dissipate the energy cascading from the larger scales. In this way, the resolution of the smallest dissipative scales is avoided, and this can potentially reduce the computational cost and/or be used to increase the Reynolds number of the simulations. Thus, the LES approach lies in between the extremes of DNS and RANS.

In this study, our primary objective is to conduct and quantify the success of LES in a stratified mixing problem. This is an important step that must be taken in order to extend LES to many small-scale mixing problems in coastal zones and the bottom boundary layers of the ocean. To this end, stratified mixing in a dam-break problem is considered, which seems to be an idealized yet effective test case for our purpose. First, it offers a number of simplifications avoiding the ambiguity of the initial and boundary conditions. Second, a geometrically simple rectangular enclosed domain is employed. Third, the system is dynamically challenging, exhibiting a complex interaction between shear-induced mixing and internal waves. The probability distribution function (p.d.f.) of equilibrium density resulting from the mixing of the initial dense and light water masses depends critically on a faithful representation of this interaction, and yields a restrictive criterion for the accuracy of the tested SGS models.

We consider variants of the Smagorinsky SGS model (Smagorinsky, 1963), which is a common choice in LES studies. Smagorinsky models have been tested extensively for homogeneous flows, and versions have been proposed (Schumann, 1975; Stevens et al., 1998; Dörnbrack, 1998) to take into consideration the effect of stratification via the local shear Richardson number, the square of the ratio of the buoyancy frequency and the vertical shear. However, these SGS models have not been tested thoroughly for stratified mixing problems. Our present study is an exploratory step in this direction.

In order to obtain benchmark solutions to assess the performance of LES, we conduct DNS. However, in light of the resolution requirements for DNS and the large number of LES to explore the parameter range, 3D computations are prohibitively expensive with the computational resources available to us (a recent 32 processor Linux cluster). Thus, all of the calculations are conducted in 2D.

The SGS models have been implemented in Nek5000, the high-order spectral element model developed by P. Fischer (Fischer, 1997; Fischer et al., 2000; Fischer and Mullen, 2001). This model combines the geometrical flexibility of finite element models with the numerical accuracy of spectral models. In this study, it is the latter advantage of this model that is important, as the geometry of the domain is simple.

The paper is organized as follows: The concept of LES and the SGS models tested in this study are discussed in Section 2. A short description of the numerical model Nek5000 is given in Section 3. The model configuration and the parameters of the numerical experiments are outlined in Section 4. Results are presented in Section 5. Finally, the principal findings and future directions are summarized in Section 6.

2. LES and SGS models

2.1. Review

The underlying idea of LES is based on the observation that most of the turbulent flows features are carried out by coherent structures (namely, large eddies). Since the characteristics of these coherent structures change significantly from one flow type to another, these eddies must be resolved through computation. Imbedded in

these large eddies are smaller eddies, which arise from the breakdown of the large eddies into turbulence. The small eddies have a much more universal character, namely they tend to act primarily to dissipate the energy cascading from the large eddies. Thus, they are much more conducive for parameterizations. Below we present a short review of LES. The reader is referred to Sagaut (2005) and Berselli et al. (2005) for an extensive review of recent LES literature.

In the case of homogeneous incompressible fluid, the Navier–Stokes equations (NSE) reduce to

$$\frac{D\mathbf{u}}{Dt} + \frac{1}{\rho_0} \nabla p - \nu \Delta \mathbf{u} = 0, \tag{1}$$

$$\nabla \cdot \mathbf{u} = 0, \tag{2}$$

where the material (total) derivative is

$$\frac{D}{Dt} = \frac{\partial}{\partial t} + \mathbf{u} \cdot \nabla, \tag{3}$$

Δ is the Laplacian operator, ρ_0 is the constant fluid density, p is the pressure, and ν is the kinematic viscosity.

In LES, the large structures (eddies) are obtained by convolving of the velocity \mathbf{u} with a filter function $g_\delta(\mathbf{x})$, namely $\bar{\mathbf{u}}(\mathbf{x}, t) := (g_\delta * \mathbf{u})(\mathbf{x}, t)$. Such an averaging suppresses any fluctuations in \mathbf{u} below the filter scale δ . Using the fact that (for constant $\delta > 0$ and in the absence of boundaries) filtering commutes with differentiation, gives the space-filtered NSE

$$\frac{\partial \bar{\mathbf{u}}}{\partial t} + \nabla \cdot (\bar{\mathbf{u}}\bar{\mathbf{u}}^T) + \frac{1}{\rho_0} \nabla \bar{p} - \nu \Delta \bar{\mathbf{u}} = -\nabla \cdot \boldsymbol{\tau}(\mathbf{u}, \mathbf{u}) \quad \text{in } \Omega \times (0, T), \tag{4}$$

$$\nabla \cdot \bar{\mathbf{u}} = 0 \quad \text{in } \Omega \times (0, T). \tag{5}$$

This system is not closed, since it involves both \mathbf{u} and $\bar{\mathbf{u}}$. The subgrid-scale stress (SGS) tensor $\boldsymbol{\tau}(\mathbf{u}, \mathbf{u}) = \mathbf{u}\mathbf{u}^T - \bar{\mathbf{u}}\bar{\mathbf{u}}^T$ ($\tau_{ij} = \bar{u}_i \bar{u}_j - \bar{u}_i \bar{u}_j$) represents the effect of the filtered scales on the resolved scales of motion. Thus, the closure problem in LES is to specify a tensor $\mathcal{S} = \mathcal{S}(\bar{\mathbf{u}}, \bar{\mathbf{u}})$ to replace $\boldsymbol{\tau}(\mathbf{u}, \mathbf{u})$ in (4).

The most popular approach in LES is the eddy viscosity (EV) model, motivated by the idea that the global effect of the subfilter-scale stress tensor $\boldsymbol{\tau}(\mathbf{u}, \mathbf{u})$, in the mean, is to transfer energy from resolved to unresolved scales through inertial interactions. EV models are motivated by Kolmogorov’s (K-41) theory (Frisch, 1995; Pope, 2000; Sagaut, 2005). The mathematical realization is the model

$$\nabla \cdot \boldsymbol{\tau}(\mathbf{u}, \mathbf{u}) \approx -\nabla \cdot (v_T \nabla^s \bar{\mathbf{u}}) + \text{terms incorporated into } \bar{p},$$

where $\nabla^s \bar{\mathbf{u}} := (\nabla \bar{\mathbf{u}} + \nabla \bar{\mathbf{u}}^T)/2$ is the deformation tensor of $\bar{\mathbf{u}}$ and $v_T \geq 0$ is the “turbulent viscosity coefficient”.

The Smagorinsky model (Smagorinsky, 1963) is a common approach in geophysical flows for calculating the turbulent viscosity coefficient $v_T(\bar{\mathbf{u}}, \delta)$,

$$v_T = v_{\text{Smag}}(\bar{\mathbf{u}}, \delta) := (c_s \delta)^2 \|\nabla^s \bar{\mathbf{u}}\|_F, \tag{6}$$

where c_s is the Smagorinsky constant, and $\|\sigma\|_F := \sqrt{\sum_{i,j=1}^d |\sigma_{ij}|^2}$ is the Frobenius norm of the tensor σ . By equating the dissipation rates $\langle \epsilon \rangle = \langle \epsilon_{\text{model}} \rangle$, where $\epsilon(t) = \frac{\nu}{|\Omega|} \|\nabla \mathbf{u}(t)\|^2$, with $|\Omega|$ being the measure (area) of the computational domain Ω , Lilly (1967) put forth (under a number of optimistic assumptions) that c_s has a universal range of ~ 0.17 . However, this theoretical range has been found to be too large in LES studies of many different types of flows, with many researchers preferring a range of $0.065 \leq c_s \leq 0.10$ instead (Wang et al., 1998; Reynolds, 1989; Moin and Kirn, 1982; Ferziger, 2005). More successful modifications of (6) include the *dynamic* SGS models (Germano et al., 1991) and the *Lagrangian dynamic* SGS model of Meneveau et al. (1996) and Porte-Agel et al. (2000).

Besides EV models, there are other successful SGS models, well surveyed in Sagaut (2005). Each one of these alternative SGS models would be worthy of investigation for oceanographic problems. However, given the complexity of our problem and the popularity of the Smagorinsky model (6) in geophysical studies (Métais, 1998; Riley and Lelong, 2000; Stevens et al., 1999; Buffett, 2003), we decided to first focus on the Smagorinsky model (6) in stratified flows. Specifically, a thorough sensitivity study of parameterizations of the Smagorinsky model for stratified flows is presented.

2.2. LES for stratified flows

Although started in the geophysics community in 1963 by Smagorinsky, LES has been developed mostly in the engineering community for the last 40 years. Thus, much of the success of LES has been built around features specific to engineering flows. Indeed, EV models, by far the most popular in LES, are entirely based on the concept of energy cascade. One of the fundamental assumptions in EV models is the *homogeneity* and *isotropy* of the underlying turbulent flow. While valid in many engineering applications, the assumption of isotropy and universality of subgrid-scales might fail in geophysical settings, where stratification plays an important role.

Thus, an essential question is: Can the SGS models developed for engineering flows be modified and used in geophysical applications with stratification? Moreover, if the answer is yes, then what is the “optimal” modification? The main challenges in our investigation are:

(A) *What are the “optimal” SGS models for*

$$\boldsymbol{\tau}(\mathbf{u}, \mathbf{u}) = \overline{\mathbf{u}\mathbf{u}} - \overline{\mathbf{u}}\overline{\mathbf{u}} \quad \text{and} \quad \boldsymbol{\sigma}(\mathbf{u}, \rho') = \overline{\mathbf{u}\rho'} - \overline{\mathbf{u}}\overline{\rho'} \quad (7)$$

in the filtered Boussinesq equations (8)–(10)?

$$\frac{D\overline{\mathbf{u}}}{Dt} + \frac{1}{\rho_0} \nabla \overline{p} - \nu \Delta \overline{\mathbf{u}} + \frac{\overline{\rho'}}{\rho_0} g \mathbf{k} = -\nabla \cdot \boldsymbol{\tau}(\mathbf{u}, \mathbf{u}), \quad (8)$$

$$\nabla \cdot \overline{\mathbf{u}} = 0, \quad (9)$$

$$\frac{D\overline{\rho'}}{Dt} - \kappa \Delta \overline{\rho'} = -\nabla \cdot \boldsymbol{\sigma}(\mathbf{u}, \rho'), \quad (10)$$

where ρ' is the density perturbation in a fluid with density $\rho = \rho_0 + \rho'$ such that $\rho' \ll \rho_0$, κ is the molecular diffusion coefficient, g is the gravitational acceleration and \mathbf{k} is the unit normal vector in the vertical direction.

(B) *What are the correct boundary conditions in the filtered Boussinesq equations (8)–(10)?*

There are essentially two ways to treat boundary conditions in LES (Pope, 2000). The first is to decrease δ to zero at the boundaries. This popular approach, known as near wall resolution (NWR), captures the important flow features near the boundary, but has a high computational cost since it requires a fine mesh near the wall. The second is referred to as near wall modeling (NWM) and is developed by using boundary layer theory. Since the discretization near boundaries can remain coarse, the NWM approach is more efficient and thus a better candidate for LES of realistic turbulent flows.

(C) *What is the optimal treatment of complex geometries?*

This is also an important challenge for LES of engineering flows without stratification. Since much of the available theory in simple geometries (such as boundary layer theory) is not extended to complex geometries (for instance, due to separation at a curved boundary), choosing “optimal” boundary conditions in the latter becomes an even harder task.

Since each of the three challenges of applying LES to stratified flows is a daunting task, we focus on the first one, namely on finding appropriate SGS models. Specifically, we chose the most popular EV model, the Smagorinsky model (Smagorinsky, 1963), and investigate it in the context of the dam-break problem. First, this approach decouples the challenges of finding optimal boundary and initial conditions and treating complex geometries from the challenge of SGS modeling in stratified flows, which is the focus in this paper. Second, the dam-break problem is dynamically challenging, exhibiting a complex interaction between shear-induced mixing and internal waves.

2.3. SGS models tested

Several modifications of the Smagorinsky model (6) have been proposed to take into account the effect of stratification via the Richardson number Ri , where

$$Ri = \frac{N^2}{\left(\frac{\partial u}{\partial z}\right)^2 + \left(\frac{\partial v}{\partial z}\right)^2} \quad (11)$$

is the ratio of the square of buoyancy frequency $N^2 = -\frac{g}{\rho_0} \frac{\partial \rho'}{\partial z}$ and vertical shear (Schumann, 1975; Stevens et al., 1998; Dörnbrack, 1998). This study presents a thorough numerical investigation of such *Ri-dependent SGS models*. The *Ri*-dependence in the filtered Boussinesq equations (8)–(10) can be included in the SGS tensor $\tau(\mathbf{u}, \mathbf{u})$ in (8), or in the SGS tensor $\sigma(\mathbf{u}, \rho')$ in (10), or both. Specifically, we consider SGS models of the following form on the right-hand-side of the filtered Boussinesq equations:

$$\frac{D\bar{u}_1}{Dt} + \frac{1}{\rho_0} \frac{\partial \bar{p}}{\partial x_1} - \nu \left(\frac{\partial^2 \bar{u}_1}{\partial x_1^2} + \frac{\partial^2 \bar{u}_1}{\partial x_2^2} + \frac{\partial^2 \bar{u}_1}{\partial x_3^2} \right) = \sum_{j=1}^3 \frac{\partial}{\partial x_j} \left[f_j(Ri) (c_s \delta)^2 \|\nabla^s \bar{\mathbf{u}}\|_F \frac{1}{2} \left(\frac{\partial \bar{u}_1}{\partial x_j} + \frac{\partial \bar{u}_j}{\partial x_1} \right) \right], \quad (12)$$

$$\frac{D\bar{u}_2}{Dt} + \frac{1}{\rho_0} \frac{\partial \bar{p}}{\partial x_2} - \nu \left(\frac{\partial^2 \bar{u}_2}{\partial x_1^2} + \frac{\partial^2 \bar{u}_2}{\partial x_2^2} + \frac{\partial^2 \bar{u}_2}{\partial x_3^2} \right) = \sum_{j=1}^3 \frac{\partial}{\partial x_j} \left[f_j(Ri) (c_s \delta)^2 \|\nabla^s \bar{\mathbf{u}}\|_F \frac{1}{2} \left(\frac{\partial \bar{u}_2}{\partial x_j} + \frac{\partial \bar{u}_j}{\partial x_2} \right) \right], \quad (13)$$

$$\frac{D\bar{u}_3}{Dt} + \frac{1}{\rho_0} \frac{\partial \bar{p}}{\partial x_3} + \frac{\bar{\rho}'}{\rho_0} g - \nu \left(\frac{\partial^2 \bar{u}_3}{\partial x_1^2} + \frac{\partial^2 \bar{u}_3}{\partial x_2^2} + \frac{\partial^2 \bar{u}_3}{\partial x_3^2} \right) = \sum_{j=1}^3 \frac{\partial}{\partial x_j} \left[f_j(Ri) (c_s \delta)^2 \|\nabla^s \bar{\mathbf{u}}\|_F \frac{1}{2} \left(\frac{\partial \bar{u}_3}{\partial x_j} + \frac{\partial \bar{u}_j}{\partial x_3} \right) \right], \quad (14)$$

$$\frac{D\bar{\rho}'}{Dt} - \kappa \left(\frac{\partial^2 \bar{\rho}'}{\partial x_1^2} + \frac{\partial^2 \bar{\rho}'}{\partial x_2^2} + \frac{\partial^2 \bar{\rho}'}{\partial x_3^2} \right) = \sum_{j=1}^3 \frac{\partial}{\partial x_j} \left[g_j(Ri) (c_s \delta)^2 \|\nabla^s \bar{\mathbf{u}}\|_F \frac{\partial \bar{\rho}'}{\partial x_j} \right], \quad (15)$$

$$\frac{\partial \bar{u}_1}{\partial x_1} + \frac{\partial \bar{u}_2}{\partial x_2} + \frac{\partial \bar{u}_3}{\partial x_3} = 0. \quad (16)$$

When stratified fluid is perturbed, two kinds of flow patterns are observed. First, internal waves can be generated that transport energy and momentum. Development of SGS models for internal waves is a challenging problem and is not attempted here. Second, mixing, namely irreversible modification of the distribution of the density field, can take place, the nature of which is regulated by the ratio of the strength of vertical shear (that generates mixing) and stratification (that tends to suppress mixing). As shown using laboratory experiments by Fernando (2000), all scales of turbulent motions are undamped by the stratification and turbulence spreads in all directions as in unstratified backgrounds in the case of small *Ri*. For large *Ri*, the stratification retards the vertical growth, producing strong anisotropy, namely horizontally elongated and vertically compressed structures. Thus, following Schumann (1975), Stevens et al. (1998) and Dörnbrack (1998), we consider a simple approach to model unresolved anisotropic mixing in stratified fluids via splitting eddy viscosities into horizontal and vertical components, and by regulating the vertical mixing via a function $f(Ri)$, which is taken here of the form (Fig. 1)

$$f(Ri) = \begin{cases} 1 & \text{for } Ri < 0, \\ \sqrt{1 - \frac{Ri}{Ri_c}} & \text{for } 0 \leq Ri \leq Ri_c, \\ 0 & \text{for } Ri > Ri_c, \end{cases} \quad (17)$$

where Ri_c is the critical threshold, typically $Ri_c = 0.25$ (Miles, 1961; Rohr et al., 1988). The rationale for this type of SGS models is that when $Ri \geq Ri_c$, shear cannot overcome stratification, and fluid mixes primarily in the horizontal plane, or in the form of so-called “pancake mixing” (Fernando, 2000). Hence, with this model we attempt to represent the characteristic anisotropic mixing in stratified flow. When $Ri = 0$, the motion is isotropic and the original Smagorinsky model is recovered. It should be mentioned that Baumert and Peters (2004) classify that the regime $0 \leq Ri < 0.25$ corresponds to that of growing turbulence, $Ri = 0.25$ to equilibrium, $0.25 < Ri \leq 0.50$ to decaying turbulence, and $Ri > 0.50$ to a regime in which turbulence collapses into internal waves. Such a detailed decomposition will be considered in a future study.

There are four types of *Ri*-dependent Smagorinsky models that we investigate, according to the different values of the factors f_j and g_j in (12)–(16)

- *Model A*: $f_j(Ri) = 1.0$ and $g_j(Ri) = 1.0$, $j = 1, 2, 3$. This is the classic Smagorinsky model for the filtered Boussinesq equations (8)–(10) (Métais, 1998; Kaltenbach et al., 1994; Siegel and Domaradzki, 1994).

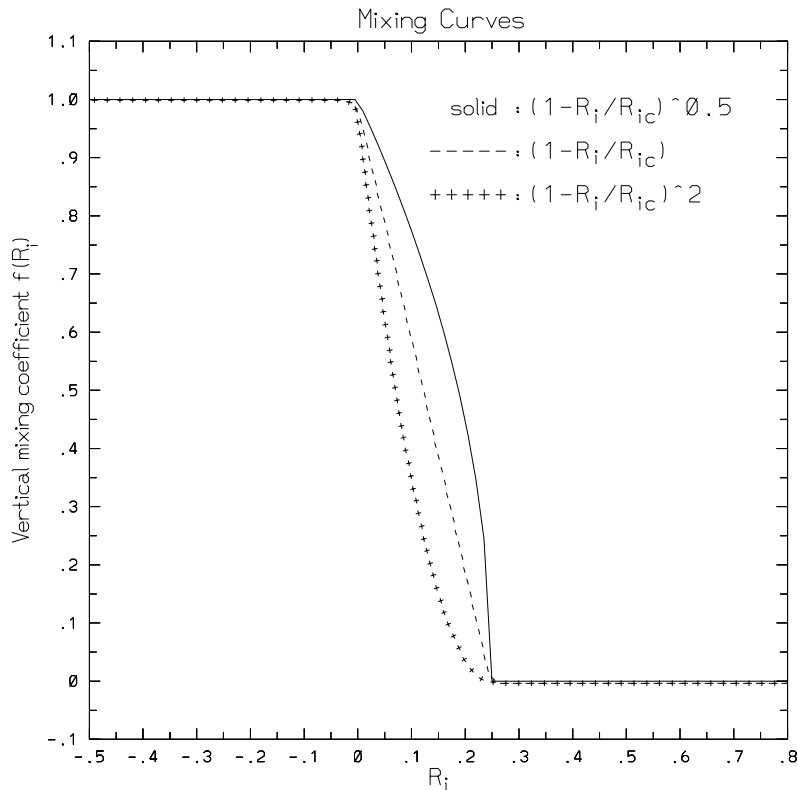


Fig. 1. The shapes of $f(Ri)$ used to introduce the anisotropy due to the effects of stratification.

- *Model B*: $f_j(Ri) = 1.0$, $j = 1, 2, 3$, $g_1(Ri) = 1.0$, $g_2(Ri) = 1.0$, and $g_3(Ri) = f(Ri)$. This is a modification of Model A in which the vertical diffusivity in (10) is Ri -dependent.
- *Model C*: $f_1(Ri) = 1.0$, $f_2(Ri) = 1.0$, $f_3(Ri) = f(Ri)$, and $g_j(Ri) = 1.0$, $j = 1, 2, 3$. This is a modification of Model A in which the vertical viscosity in (8) is Ri -dependent.
- *Model D*: $f_1(Ri) = 1.0$, $f_2(Ri) = 1.0$, $f_3(Ri) = f(Ri)$, $g_1(Ri) = 1.0$, $g_2(Ri) = 1.0$, and $g_3(Ri) = f(Ri)$. This is a modification of Model A in which both the vertical viscosity in (8) and the vertical diffusivity in (10) are Ri -dependent.

Other SGS models that take into account the effect of stratification should be mentioned to put the present study in a proper context. Deardorff (1974) proposed so-called differential model, which relies on the integration of the equations of SGS stresses (7). But this approach requires solution of ten additional prognostic equations (in 3D). Schmidt and Schumann (1989) developed a model that can be interpreted as a simplification of the Deardorff (1974) model. Subject to a number of approximations, the computation of the SGS stresses reduces to the integration of a single prognostic equation for subgrid kinetic energy. SGS models by Deardorff (1974) and Schmidt and Schumann (1989) do not rely on the eddy diffusivity/viscosity paradigm, and are fully anisotropic. Deardorff (1980) put forth another SGS model based on integration of a prognostic equation for subgrid kinetic energy and the eddy diffusivity/viscosity assumption. In oceanographic applications of LES, Wang et al. (1996) studied equatorial turbulence using an SGS model, in which the eddy diffusivity and eddy viscosity are related to Ri based on formulations put forth by Pacanowski and Philander (1981) and Peters et al. (1989). Wang et al. (1998) revisited this problem using an SGS model based on turbulent length scales in stratified flows from the study by Schumann (1991). Raasch and Etling (1998) studied deep convection by employing the SGS model put forth by Deardorff (1980). Skillingstad et al. (1999) and Skillingstad and Wijesekera (2004) investigated upper ocean turbulence during wind bursts and flows over 2D obstacles, respectively, using a Smagorinsky class SGS model, in which the eddy diffusivity is related to the

eddy viscosity via a proportionality constant represented by a turbulent Prandtl number. There appears to be a general trend of employing simpler SGS models in LES studies, probably due to a larger spectrum of resolved scales with the increasing computer power.

3. Numerical model

Nek5000 combines the high-order accuracy of spectral methods with the geometric flexibility of traditional finite element methods. The code integrates unsteady incompressible Navier–Stokes equations within Boussinesq approximation. Moreover, Nek5000 handles general three-dimensional flow configurations, supports a broad range of boundary conditions for hydrodynamics, and accommodates multiple-species (passive or active tracer) transport. Here, we give a short description of this code.

The time advancement of (12)–(16) is based on second-order semi-implicit operator-splitting methods developed by Maday et al. (1990) and described by Fischer (1997). The hydrodynamics are advanced first, with explicit treatment of the buoyancy forcing term, followed by the update of the salinity transport. Spatial discretization is based on the spectral element method (Patera, 1984; Maday and Patera, 1989; Fischer, 1997), which is a high-order weighted residual technique based on compatible velocity and pressure spaces free of spurious modes. Locally, the spectral element mesh is structured, with the solution, data, and geometry expressed as sums of N th-order Lagrange polynomials on tensor-products of Gauss or Gauss–Lobatto quadrature points. Globally, the mesh is an unstructured array of K deformed hexahedral elements and can include geometrically nonconforming elements. For problems having smooth solutions, the spectral element method achieves exponential convergence with N , despite having only C^0 continuity (which is advantageous for parallelism). The convection operator exhibits minimal numerical dissipation and dispersion, which is important for high-Reynolds number applications.

Efficient solution of the Navier–Stokes equations in complex domains depends on the availability of fast solvers for sparse linear systems. Nek5000 uses as a preconditioner the additive overlapping Schwarz method introduced by Dryja and Widlund (1987) and developed in the spectral element context by Fischer (1997) and Fischer et al. (2000). The key components of the overlapping Schwarz implementation are fast local solvers that exploit the tensor-product form and a parallel coarse-grid solver that scales to thousands of processors (Tufo and Fischer, 2001). The capabilities of the spectral element method have been significantly enhanced through the recent development of a high-order filter that stabilizes the method for convection dominated flows without compromising spectral accuracy (Fischer and Mullen, 2001).

Nek5000 has been used in the numerical investigation of SGS models in turbulent channel flows, where SGS models of both EV and Approximate Deconvolution types were considered (Iliescu and Fischer, 2003, 2004). The code has also been used for various bottom gravity current simulations (Özgökmen et al., 2004a,b; Özgökmen and Johns, 2006), and these results have been subsequently used to refine parameterizations of gravity current mixing for an ocean general circulation model (Chang et al., 2005).

4. Model configuration and parameters

The first step in the experimental strategy is to select the model domain and parameters, as well as the geometry of the domain, the initial and boundary conditions. To this end, a simple rectangular domain of $-\frac{1}{2} \leq x \leq \frac{1}{2}$ and $0 \leq z \leq H$ is selected, in which the aspect ratio of horizontal and vertical dimensions of the domain is $a = L/H = 5$. An aspect ratio $a \gg 1$ is required in order to obtain high shear across the density interface, and to transition to Kelvin–Helmholtz (KH) instability. It is well-known that the necessary condition for the formation of KH instability is given by the criteria $Ri \leq 0.25$ (Miles, 1961). In a domain with large a , the density interface has more space to tilt and stretch, satisfying this criteria at multiple locations, which leads to the formation of multiple KH rolls.

In order to reduce the number of parameters, the Boussinesq equations (8) and (10) in the case of DNS (without filtering and SGS stress terms) can be nondimensionalized by using

$$\mathbf{u} = U_0 \mathbf{u}^*, \quad \mathbf{x} = \ell \mathbf{x}^*, \quad t = \frac{\ell}{U_0} t^*, \quad p = \rho_0 U_0^2 p^*, \quad \rho' = \Delta \rho' \rho'^*, \quad (18)$$

where U_0 and ℓ are characteristic speed and length scales of the problem, and $\Delta\rho'$ is the density difference between the two main water masses. Here, U_0 will be taken as the initial gravity current speed (defined below) and $\ell = H/2$ the average thickness of the two (bottom and surface) gravity currents. Dropping “*” for nondimensional variables, yields

$$\frac{D\mathbf{u}}{Dt} + \nabla p - \frac{1}{Re} \Delta \mathbf{u} + \frac{1}{Fr^2} \rho' \mathbf{k} = 0, \quad (19)$$

$$\frac{D\rho'}{Dt} - \frac{1}{RePr} \Delta \rho' = 0, \quad (20)$$

where the nondimensional parameters are the Reynolds number $Re = U_0 \ell/\nu$, the Prandtl number $Pr = \nu/\kappa$, and the Froude number $Fr = U_0/\sqrt{g\Delta\rho'\ell/\rho_0}$. However, in the case of the dam-break problem, U_0 is not externally imposed, but determined internally. The propagation speed of an internal wave in a two-layer system is given by $U_0 = \sqrt{g\Delta\rho'h(H-h)/(\rho_0H)}$, and since $h = H/2$ here, the initial gravity current speed is well approximated by $U_0 = \frac{1}{2}\sqrt{g\Delta\rho'H/\rho_0}$. Therefore, the Froude number is set to $Fr = 2^{-\frac{1}{2}}$. The Prandtl number is taken as $Pr = 7$, which corresponds to that of heat and water. Saline water has a Pr that is two orders of magnitude greater, which imposes high requirements on the numerical resolution, and thus is avoided. The primary free parameter of this system is Re and experiments are conducted at two different Reynolds numbers, $Re = 2800$ and $Re = 4300$.

Experiments are conducted using several resolutions for each set of Re (Table 1). For the case with $Re = 2800$, DNS are conducted at two resolutions to verify convergence, with number of grid points $n = 172,800$ and $n = 270,000$, denoted mid-res2 and high-res, respectively. LES are run at these resolutions, as well as at three coarser resolutions with $n = 76,800$, $n = 10,800$ and $n = 7500$, denoted mid-res1, low-res2 and low-res1, respectively. In all SGS models, $c_s = 0.05$ is used. The primary purpose is to explore whether LES can reproduce mixing accurately at these coarser resolutions, which is important in terms of computational gain. Also, so-called DNS* are conducted at these three low resolutions, in which turbulence is under-resolved and SGS stress models are not used. The purpose of these simulations is to help quantify the effect of the SGS models at these resolutions. A similar set of experiments are conducted for the case with $Re = 4300$, but at higher resolutions, going up to so-called ultra-res with $n = 1,040,400$. The reader is referred to Table 1 for details on the decomposition between the number of elements K and polynomial order N used in the experiments.

One of the inherent time scales in the system is the buoyancy period $T_b = 2\pi N_\infty^{-1}$, where $N_\infty = \sqrt{\frac{g}{\rho_0} \frac{\Delta\rho'}{H}}$ is the buoyancy frequency based on the density difference over the total vertical extent H of the system. The total

Table 1
Table of the spatial resolutions used in the 2D numerical experiments

Resolution	$Re = 2800, Pr = 7$	$Re = 4300, Pr = 7$
low-res1 $K = 300; N = 5; 7500$ points	DNS*, LES	DNS*, LES
low-res2 $K = 300; N = 6; 10,800$ points	DNS*, LES	DNS*, LES
mid-res1 $K = 1200; N = 8; 76,800$ points	DNS*, LES	DNS*, LES
mid-res2 $K = 1200; N = 12; 172,800$ points	DNS, LES	DNS*, LES
high-res $K = 1200; N = 15; 270,000$ points	DNS, LES	DNS, LES
ultra-res $K = 3600; N = 17; 1,040,400$ points	–	DNS

DNS* denotes under-resolved simulations without SGS stress models. The most computationally efficient experiment, low-res1 DNS* took about 2 h on four processors, while the most computationally expensive experiment, ultra-res DNS, took about 10 days on 32 processors. The computation time is proportional to KN^3 .

integration period T needs to be much larger than T_b for the effects of stratification to fully develop, and in this study, integrations are terminated at $T/T_b \approx 18$. This corresponds to 50,000 time steps in low-res and mid-res experiments, and 100,000 time steps in high-res and ultra-res experiments. Another important time scale in this system is the time it takes for the gravity currents to reach the walls on either side of the domain. It is found that many successive encounters of the gravity currents with the walls are required before the mixing regime subsides and the motion is primarily dominated by linear (non-mixing) internal waves. The integration time T corresponds to approximately seven full travel cycles (over $2L$) of the gravity currents.

The initial condition is one of state of rest, in which the dense fluid on the left is separated from the light fluid on the right by a sharp transition layer

$$\frac{\rho'(x, t = 0)}{\Delta\rho'} = \begin{cases} 1 & \text{for } -\frac{L}{2} \leq x < -\frac{L}{20}, \\ \frac{L}{2} - 10x & \text{for } -\frac{L}{20} \leq x < +\frac{L}{20}, \\ 0 & \text{for } +\frac{L}{20} \leq x \leq +\frac{L}{2}. \end{cases} \quad (21)$$

Since the tilting of the density interface puts the system gradually into motion, the system can be started from a state of rest.

The boundary condition for the density perturbation ρ' is no-flux (insulation). For the velocity components, no-flow and *free-slip* boundary conditions are used. The selection of these boundary conditions warrants a detailed discussion. There are currently two types of boundary conditions in LES, reviewed by [Piomelli and Balaras \(2002\)](#). The first type of boundary conditions, by far the most popular, is called *near wall resolution (NWR)* ([Pope, 2000](#)). In NWR, the filter radius δ is variable and shrinks to 0 as we approach the boundary: $\delta = \delta(\mathbf{x}) \rightarrow 0$ as $\mathbf{x} \rightarrow \partial\Omega$. The main drawback of NWR is its high computational cost. Indeed, near the boundary, NWR becomes for all practical purposes a DNS. The analysis in ([Chapman, 1979](#)), in which it is shown that the cost of NWR increases very steeply with Re , is very illuminating. Another drawback of NWR is that it uses a variable filter radius $\delta(\mathbf{x})$. Since differentiation and convolution do not commute ([Aldama, 1990](#)), this introduces the *commutation error*, which can be significant and needs to be accounted for in the LES model ([Fureby and Tabor, 1997](#); [Vasilyev et al., 1998](#); [Marsden et al., 2002](#); [van der Bos and Geurts, 2005](#)). The second type of boundary conditions is called *near wall modeling (NWM)*. In NWM, the filter radius δ is kept constant near the boundary. Since the discretization in the wall region can remain coarse, NWM is significantly more efficient than NWR. Moreover, since δ is constant throughout the computational domain, the commutation error introduced by NWR is not present in NWM. NWM, however, introduces different challenges. Since δ is constant throughout the domain, we need to address filtering through the boundaries. In this case, the LES model should include an approximation for the *boundary commutation error (BCE)*, which appears as a result of extending (nonsmoothly) the flow variables outside Ω in order to be able to convolve them with the spatial filter g_δ ([Berselli et al., 2005](#)). The BCE is significant ([Vasilyev et al., 1998](#); [Dunca et al., 2004](#)) and should be approximated by the LES model. Since the BCE involves the stress tensor $2\mu\mathbb{D}(\mathbf{u}) - p\mathbb{I}$ of the true (*unfiltered*) flow variables evaluated on the boundary, the approximation of BCE in the LES model is challenging ([Das and Moser, 2001](#); [Borggaard et al., 1995](#)). In NWM, boundary layer theory provides the physical insight necessary to account for the information below the filter scale δ . This boundary layer theory might simply not hold in complex geophysical settings involving stratification.

Both NWR and NWM have significant advantages and drawbacks. Given the computational complexity of oceanographic settings, we decided to choose the more efficient NWM, in which the filter radius δ is kept constant throughout the domain. Specifically, we chose *no-flux* (insulation) boundary conditions for the density perturbation and *no flow* and *free slip* boundary conditions for the velocity components

$$\frac{\partial u}{\partial \mathbf{n}} = 0; \quad \frac{\partial w}{\partial \mathbf{n}} = 0; \quad (u, v, w) \cdot \mathbf{n} = 0; \quad \frac{\partial \rho'}{\partial \mathbf{n}} = 0, \quad (22)$$

with \mathbf{n} being the normal to the boundary.

For the SGS models A–D, we considered the following boundary conditions:

$$\frac{\partial \bar{u}}{\partial \mathbf{n}} = 0; \quad \frac{\partial \bar{w}}{\partial \mathbf{n}} = 0; \quad (\bar{u}, \bar{v}, \bar{w}) \cdot \mathbf{n} = 0; \quad \frac{\partial \bar{\rho}'}{\partial \mathbf{n}} = 0. \quad (23)$$

The boundary conditions (23) are quite accurate in the flow regions away from the density interface (see Fig. 2). Indeed, in these regions the flow variables are approximately constant in the wall-normal direction. Thus, for example, if $\partial u/\partial \mathbf{n} = 0$, then $\partial \bar{u}/\partial \mathbf{n} = 0$ will be an accurate approximation. Around the density interface, however, these boundary conditions are less accurate, especially for large values of the filter radius δ .

We preferred the boundary conditions (23) to the more popular Dirichlet boundary conditions, since NWM for the latter would have been significantly more difficult. Indeed, starting with $\mathbf{u} = \mathbf{0}$ and filtering with a spatial filter with large δ , would yield $\bar{\mathbf{u}} \neq \mathbf{0}$. Thus, since the boundary layer theory available in NWM of turbulent flows without stratification is not available in our setting, approximating $\bar{\mathbf{u}}$ on the boundary would be challenging. Finding the “right” boundary conditions is one of the main challenges in LES, even for flows without stratification. In this study we tried to avoid as much as possible this challenge and focus on the closure problem, that is, finding optimal SGS models for stratified flows. Optimal boundary conditions for LES of stratified flows will be the subject of a future study.

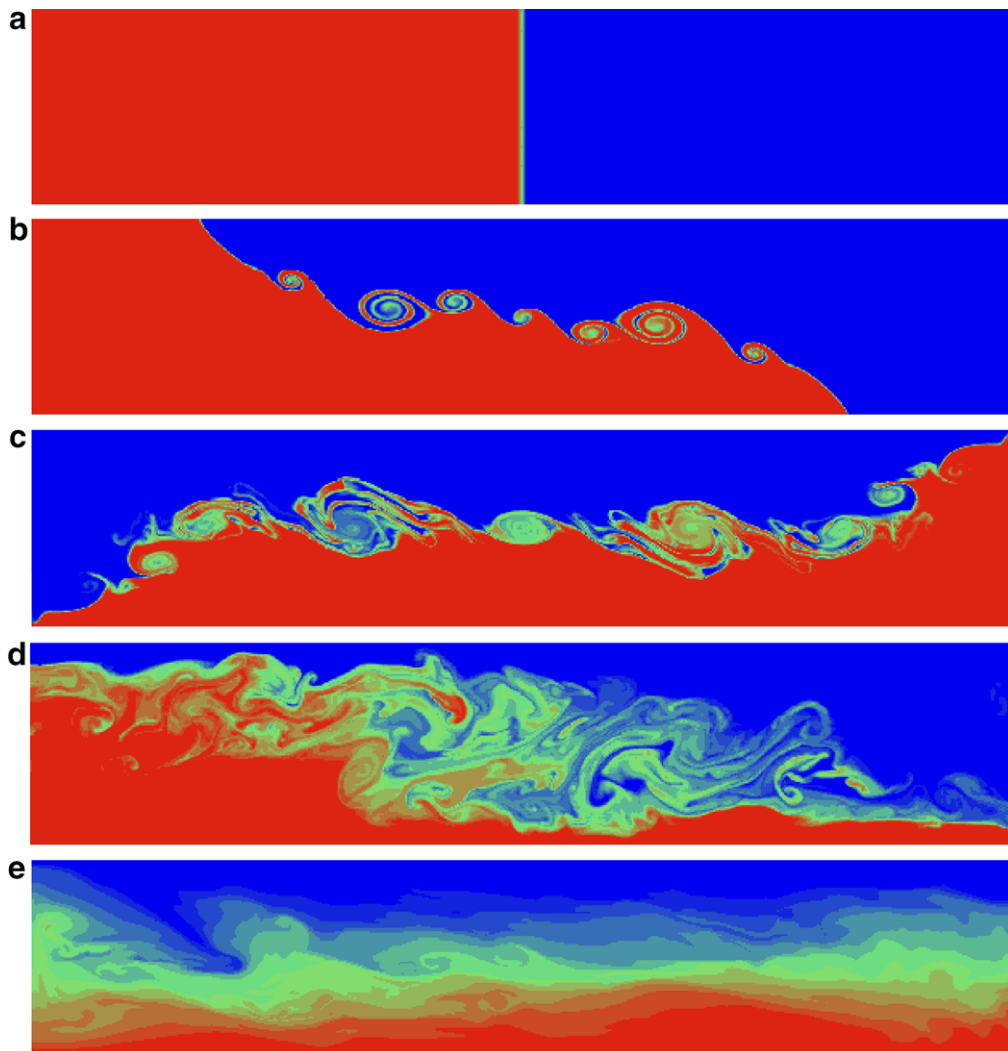


Fig. 2. Distribution of the density perturbation $\rho'(x,z,t)/\rho_0$ at (a) $t = 0$, (b) $t/T_b = 0.57$, (c) $t/T_b = 1.17$, (d) $t/T_b = 4.00$, and (e) $t/T_b = 16.20$ in high-res DNS for $Re = 2800$. The animation of this simulation is available from <http://www.rsmas.miami.edu/personal/tamay/3D/DNS-2d-highres.gif>.

5. Results

5.1. DNS results

5.1.1. Description

The time-evolution of the system is illustrated using several snapshots of the density perturbation from high-res DNS for $Re = 2800$ in Fig. 2. The system starts with the density perturbation distribution given by (21) (Fig. 2a), and rapidly forms characteristic KH billows along the interface of counter-propagating gravity currents (Fig. 2b, e.g. Keulegan, 1958, Simpson, 1987). KH billows grow by entrainment of ambient fluid as well as by pairing, and the gravity currents are reflected from the side walls (Fig. 2c). Gradually, the nature of the mixing becomes much more complex and individual KH billows cannot be identified anymore (Fig. 2d). Towards the end of the integration period, shear-induced mixing diminishes, leaving behind an intermediate water mass with a density perturbation range that did not exist in a significant amount at the initial time (Fig. 2e).

The time-evolution of the density perturbation for $Re = 4300$ in ultra-res DNS is depicted in Fig. 3, and as a function of resolution in Fig. 4. Comparison of Figs. 4 and 3a indicate that the number of KH billows is underrepresented in low-res2 DNS*, there is a significant phase error in mid-res1 DNS*, and a minor phase error in mid-res2 DNS*. The difference between high-res DNS (Fig. 4d) and ultra-res DNS (Fig. 3a) seems quite small, such that it can be assumed that numerical convergence is achieved.

5.1.2. Energetics

In order to better understand the entire evolution of this system, it is instructive to consider the following examples. The initial density distribution (Fig. 5a) is approximately given by (neglecting the sharp transition layer)

$$\frac{\rho'_0}{\Delta\rho'} \approx \begin{cases} 1 & \text{for } -\frac{L}{2} \leq x < 0, \\ 0 & \text{for } 0 \leq x \leq \frac{L}{2}. \end{cases} \quad (24)$$

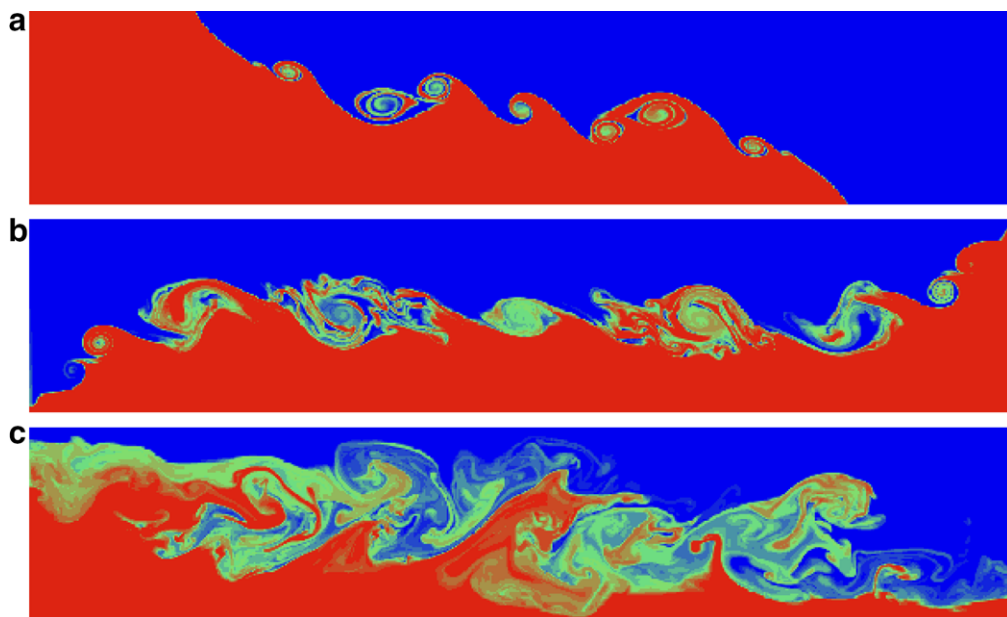


Fig. 3. Distribution of the density perturbation $\rho'(x, z, t)/\rho_0$ at (a) $t/T_b = 0.57$, (b) $t/T_b = 1.17$, and (c) $t/T_b = 4.31$ in ultra-res DNS for $Re = 4300$. The animation of this simulation is available from <http://www.rsmas.miami.edu/personal/tamay/3D/DNS-2d-ultrares.gif>.

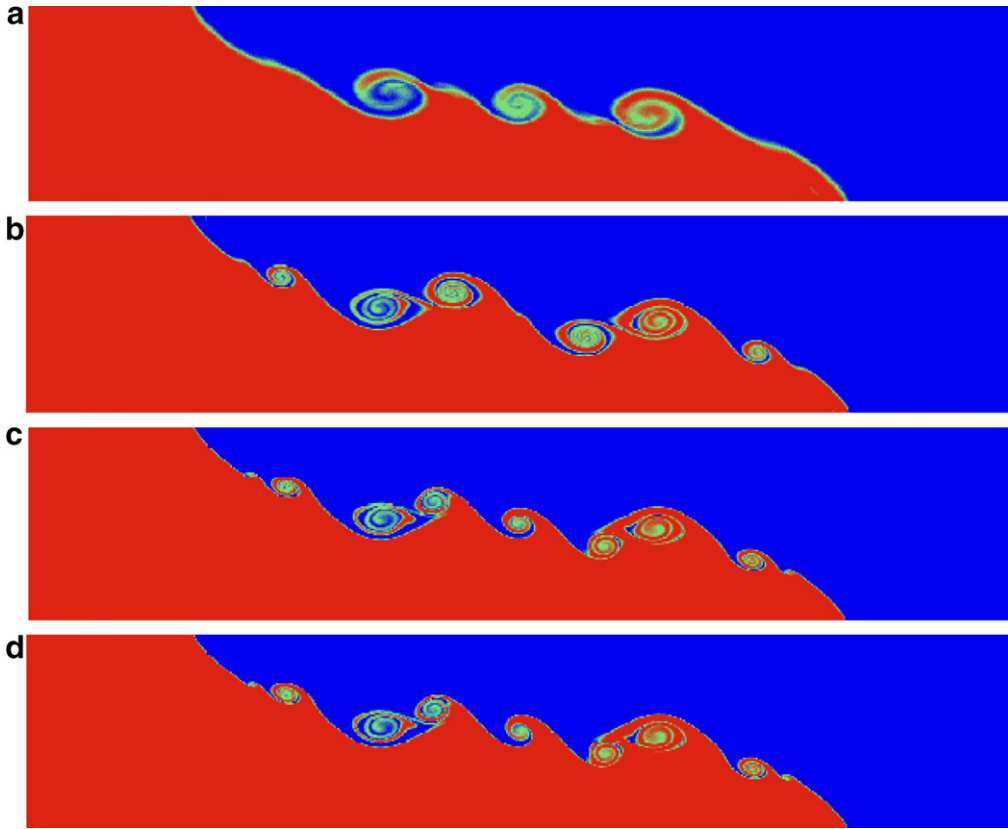


Fig. 4. Snapshots of the density perturbation distribution at $t/T_b = 0.57$ in experiments with different resolutions, (a) low-res2 DNS*, (b) mid-res1 DNS*, (c) mid-res2 DNS*, (d) high-res DNS for $Re = 4300$.

Thus, the initial potential energy is

$$PE_0 = g \int_A \rho'_0 z dA = \frac{1}{4} g \Delta \rho' L H^2 \quad (25)$$

and the initial kinetic energy $KE_0 = \frac{1}{2} \int_A |\mathbf{u}_0|^2 dA = 0$, as stated above. Next, let us assume that this system tilts over without mixing (adiabatically) such that the density distribution becomes (Fig. 5b)

$$\frac{\rho'_b}{\Delta \rho'} \approx \begin{cases} 1 & \text{for } 0 \leq z < \frac{H}{2}, \\ 0 & \text{for } \frac{H}{2} \leq z \leq H, \end{cases} \quad (26)$$

and hence

$$PE_b = \frac{1}{8} g \Delta \rho' L H^2 = \frac{PE_0}{2}. \quad (27)$$

This state corresponds to one of minimum potential energy attainable through an adiabatic distribution of ρ'_0 (so-called background state of potential energy). Thus, the available potential energy APE in the original state is (Winters et al., 1995)

$$APE_0 = PE_0 - PE_b = \frac{1}{8} g \Delta \rho' L H^2, \quad (28)$$

indicating that half of the total initial energy can be transferred to kinetic energy for carrying out turbulent mixing. Let us assume that some of this kinetic energy is used to mix the system partially over a distance of 2ℓ (Fig. 5c)

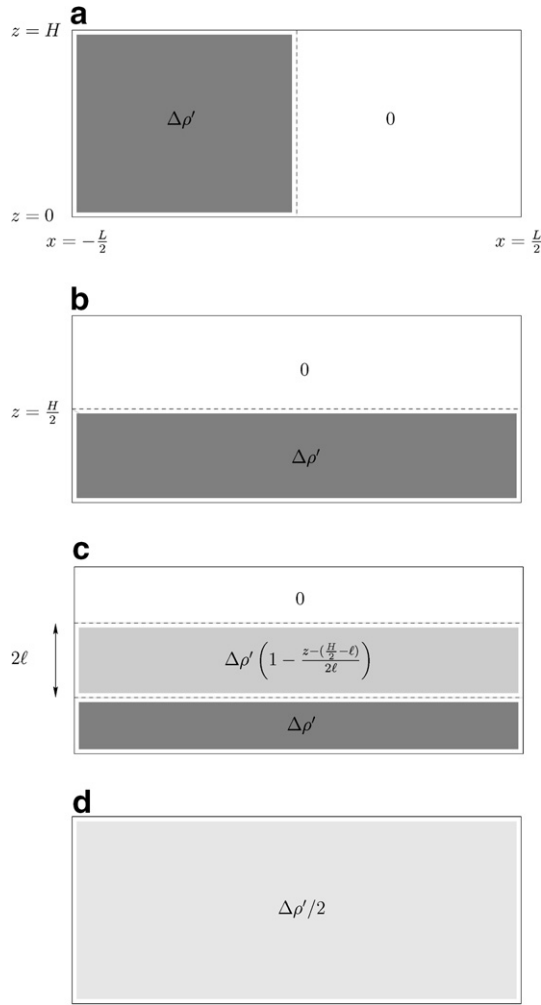


Fig. 5. Schematic diagrams of (a) the initial condition of the system, (b) tilting without mixing, (c) the partially mixed case, and (d) the homogenized system.

$$\frac{\rho'_p}{\Delta\rho'} \approx \begin{cases} 1 & \text{for } 0 \leq z < \frac{H}{2} - \ell, \\ 1 - \frac{z - (\frac{H}{2} - \ell)}{2\ell} & \text{for } \frac{H}{2} - \ell \leq z < \frac{H}{2} + \ell, \\ 0 & \text{for } \frac{H}{2} + \ell \leq z \leq H, \end{cases} \quad (29)$$

then

$$PE_p = g\Delta\rho' L \left(\frac{H^2}{8} + \frac{l^2}{6} \right). \quad (30)$$

Another possibility is that mixing extends over the entire vertical scale ($\ell = H/2$) such that a linear density profile is obtained

$$\frac{\rho'_t}{\Delta\rho'} = 1 - \frac{z}{H}, \quad (31)$$

then

$$PE_f = \frac{1}{6}g\Delta\rho' LH^2 = \frac{4}{3}PE_b. \quad (32)$$

Thus, the background potential energy has been increased by an irreversible redistribution of p.d.f. of ρ' via diapycnal mixing. Given the absence of external forcing, eventually the system has to achieve a fully homogeneous state of (Fig. 5d)

$$\frac{\rho'_h}{\Delta\rho'} = \frac{1}{2} \quad (33)$$

and

$$PE_h = PE_0, \quad (34)$$

where all APE is consumed to fully mix the system.

Several snapshots of horizontally averaged density profiles in high-res DNS for $Re = 2800$ are shown in Fig. 6, when the density interface is approximately level. By the time the counter-flowing gravity currents encounter the side walls for the first time ($t/T_b = 0.85$), turbulent processes already create a zone of $\ell \approx H/4$. After a few more internal oscillations, an approximately linear density gradient is achieved ($t/T_b = 5.70$), which remains unchanged until the end of the integration. This can be understood by approximating the local gradient Ri by a bulk Richardson number

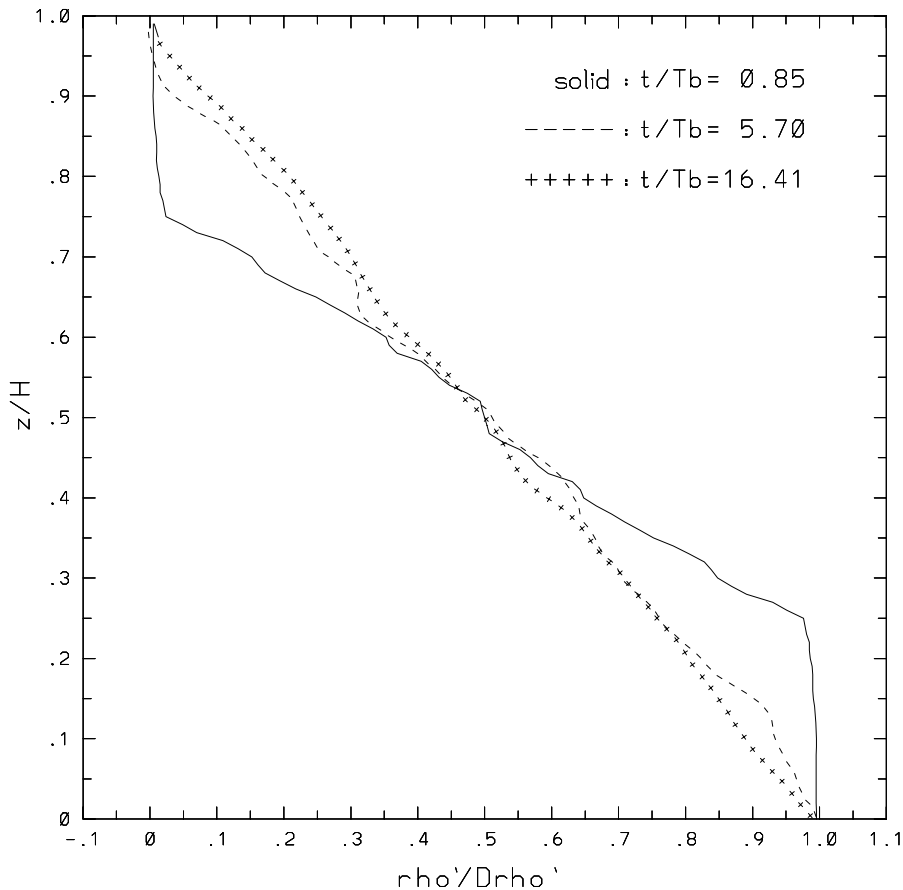


Fig. 6. Snapshots of horizontally averaged density profiles $\langle \rho'(y, t) \rangle / (\Delta\rho')$ at $t/T_b = 0.85$ (solid line), $t/T_b = 5.70$ (dashed line) and $t/T_b = 16.41$ (line with “++++”), when the density interface is approximately level in high-res DNS for $Re = 2800$. Note the fast evolution to an approximately linear profile, and the subsequent reduction in the rate of mixing.

$$Ri_b = \frac{g}{\rho_0} \frac{\Delta\rho'}{2\ell} \frac{1}{\left(\frac{\Delta u}{2\ell}\right)^2}, \quad (35)$$

where

$$\Delta u \approx 2U_0 = \sqrt{g\Delta\rho'H/\rho_0}. \quad (36)$$

Hence

$$Ri_b \approx \frac{2\ell}{H}, \quad (37)$$

which indicates that initially (21), $Ri_b \approx 0.1$ and mixing can take place in the form of KH rolls. When a density profile in the form of (31) is achieved, $Ri_b \approx 1$ and KH instability is mostly diminished. It should be noted that while turbulent overturning due to KH mode is quite strong for $Ri_b < 1$, it can persist in a weaker intensity until about $Ri_b \approx 5$ (Strang and Fernando, 2001). For $Ri_b > 5$, so-called Hölmboë waves (Hölmboë, 1962) can cause significant mixing (cf. Fig. 5 in Strang and Fernando, 2001) provided that the thickness of the shear layer is greater than that of the stratified layer. In our simulations, Hölmboë waves are not observed since the shear layer and stratified layer are of equal thickness by the time sufficiently high Ri_b is obtained for the formation of such waves. In the regime of $0.25 \leq Ri_b \leq 1$, most of the mixing is induced by the encounters of nonlinear internal waves with the side walls, and reduction of Ri during the reflection. This process appears to be responsible for a fast erosion of the density gradient during the initial stages of the simulations (Fig. 6). Once $Ri_b \approx 1$ is achieved, turbulent mixing occurs episodically and to a much lesser degree, by the complex motion of the internal waves.

The complete potential energy cycle of this system appears to be of the following sequence:

$$PE_0 \rightarrow PE_f \Rightarrow PE_h, \quad (38)$$

where the transition from the first stage (PE_0) to the second (PE_f) is characterized by turbulent mixing via features in the flow field of KH rolls and nonlinear internal waves interacting with the side walls, and this is the focus of this investigation. The transition from the second to the third stage (PE_h) takes place by molecular diffusion, namely by conversion of internal energy to potential energy. But this is a dramatically slower, weaker and simpler process, and is beyond the scope of this paper.

5.1.3. Mixed water mass fractions

Given the presence of internal waves in an enclosed domain, the system continuously exhibits transfer of energy between PE and KE. It is important to find a reliable measure to be able to judge the performance of the SGS models in LES. To this end, we follow an approach is usually referred to as *a posteriori* testing, implying the fact that the LES model is effectively tested in an actual numerical simulation. This is in contrast with *a priori* testing, where results from a fine DNS are filtered and then used to compute the LES approximation τ^{LES} (e.g., $\tau^{\text{LES}} = -\nu_T(\nabla^s \bar{\mathbf{u}})\nabla^s \bar{\mathbf{u}}$ for eddy-viscosity models) to the “true” subfilter-scale stress tensor $\tau = \bar{\mathbf{u}\mathbf{u}} - \bar{\mathbf{u}}\bar{\mathbf{u}}$. The closer τ^{LES} to τ , the better the LES model. It should be emphasized that the *a posteriori* testing is the final means of validating and testing an LES model, while the *a priori* testing represents just a step in this process. Note that there exist LES models that perform very well in *a priori* tests, while performing poorly in *a posteriori* tests (classical scale-similarity models are such an example). Thus, the more robust *a posteriori* testing is directly employed.

Here, a simple diagnostic measure is used based on the observation that the system starts from an initial condition (21), in which 49.5% of the water masses has a density perturbation of $\rho' = 0$ and another 49.5% has $\rho'/\Delta\rho' = 1$ (Fig. 2a). The fraction of the water mass with an intermediate density perturbation grows in time purely as a result of mixing between these two primary water masses (Fig. 2e). Thus, the time evolution of the fraction of mixed water masses can serve as an effective measure to diagnose exactly the net effect of the mixing process.

Fig. 7 depicts the time evolution of the fractions of water masses in various density classes in high-res DNS for the case with $Re = 2800$. First, the entire range is divided into six density bins, i.e. $0 \leq \frac{\rho'}{\Delta\rho'} < \frac{1}{6}; \dots; \frac{5}{6} \leq \frac{\rho'}{\Delta\rho'} \leq 1$. The growth in time of the fractions of the intermediate density water masses, ρ'_2 to

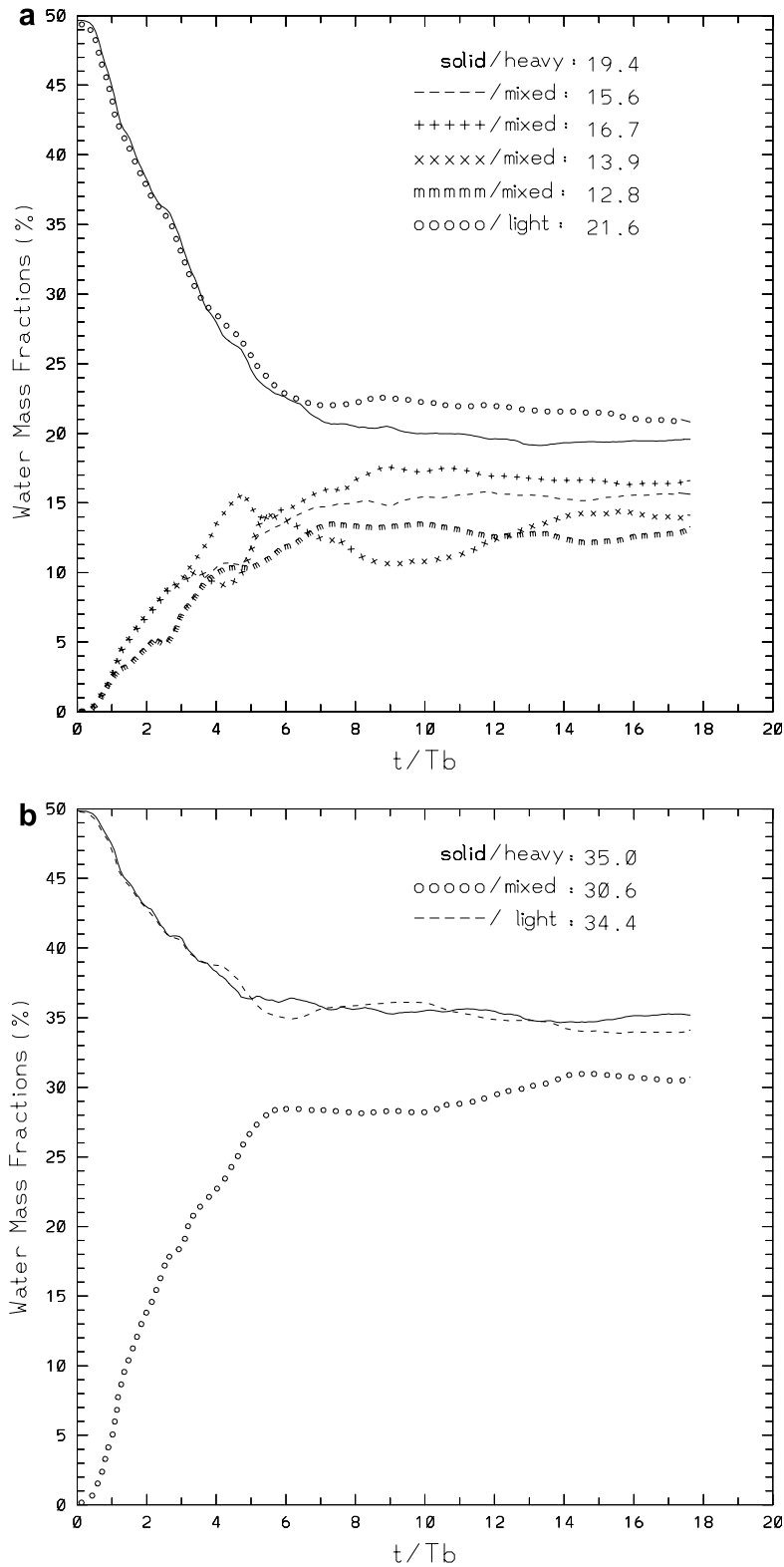


Fig. 7. Time evolutions of water mass fractions (in %) using (a) six segments, and (b) three segments in high-res DNS for $Re = 2800$. The time-averaged fractions over $12 \leq \frac{t}{T_b} \leq 18$, or equilibrium p.d.f. of ρ' are also indicated in the figure.

ρ'_5 , at the expense of the light (ρ'_1) and dense (ρ'_6) ones is clearly shown in Fig. 7a. In other words, this figure depicts the time evolution of the p.d.f. of ρ' and indicates that the irreversible diapycnal mixing changes the p.d.f. of ρ' such that the initially bipolar distribution transforms gradually to an approximately uniform distribution for the intermediate density classes. The rate of the generation of mixed water masses tapers off after $t/T_b > 6$ when a linear horizontally averaged density profile is achieved (Fig. 6) reducing Ri_b , and shear-induced mixing is replaced by non-mixing internal wave motion. The distribution of water masses in individual density classes reaches an approximate steady state in the second half of the simulation, namely for $t/T_b > 9$. Comparison of these curves in lower resolution (low-res2, mid-res1, mid-res2) DNS (not shown) reveals significant differences in equilibrium p.d.f. of ρ' , indicating that this is a stringent and discriminating technique to evaluate the state of mixing in this system. However, working with six different water masses introduces a high number of degrees of freedom regarding the evaluation of the mixing. Alternatively, only three density classes can be considered, $0 \leq \frac{\rho'_1}{\Delta\rho'} < \frac{1}{3}$, $\frac{1}{3} \leq \frac{\rho'_2}{\Delta\rho'} < \frac{2}{3}$, $\frac{2}{3} \leq \frac{\rho'_3}{\Delta\rho'} \leq 1$, as shown in Fig. 7b. Here, $\rho'_1(t)$ and $\rho'_3(t)$ follow one another closely (probably because of the linearity of the Boussinesq equations with respect to ρ'), and mixed density class $\rho'_2(t)$ is generated at their expense, with water mass fractions stabilizing at $\approx 35\%$ for $\rho'_1(t)$ and $\rho'_3(t)$, and at $\approx 30\%$ for $\rho'_2(t)$ at the approximate steady state. Given the symmetric behavior of $\rho'_1(t)$ and $\rho'_3(t)$, it seems sufficient to employ only $\rho'_2(t)$ to differentiate the results of mixing. It is shown in Section 5.2 using all six density classes that this leads to an adequate characterization of the state of mixing in this system.

The time evolution of the volume fraction of water masses in the density class $\frac{1}{3} \leq \frac{\rho'_2}{\Delta\rho'} < \frac{2}{3}$ in experiments with different resolutions (low-res2, mid-res1, mid-res2) DNS are illustrated in Fig. 8. The $\rho'_2(t)$ curve from high-res DNS is taken as the benchmark to test the SGS models in LES. The corresponding curves for $Re = 4300$ are shown in Fig. 9, in which case $\rho'_2(t)$ curve from ultra-res DNS is taken as the benchmark. It is important to note that low-res1 DNS* for $Re = 2800$, and both low-res1 and low-res2 DNS* for $Re = 4300$

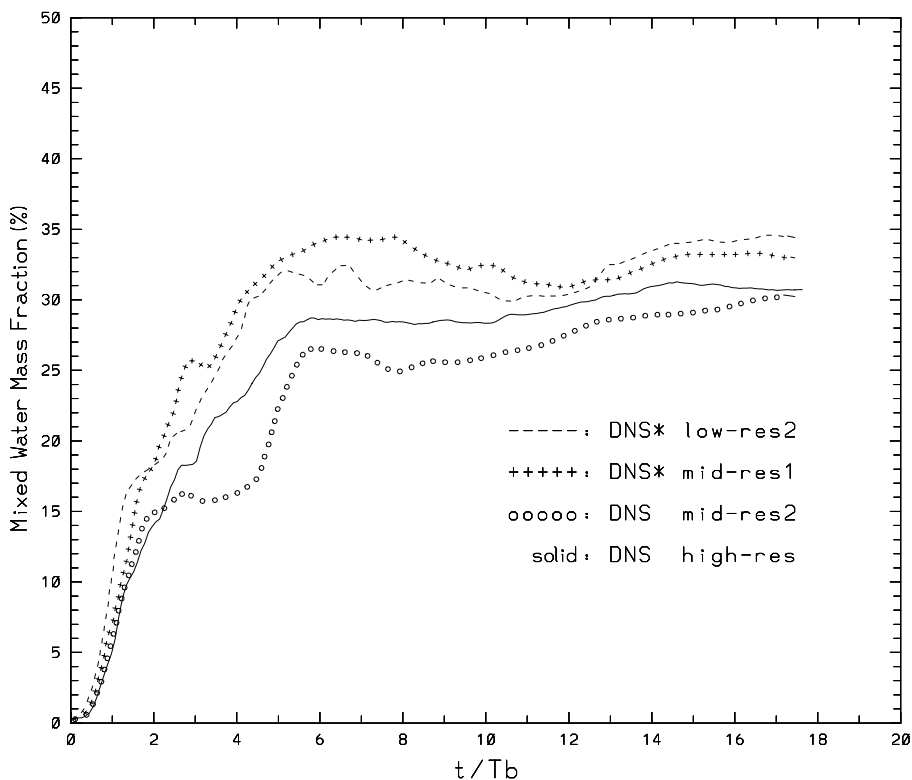


Fig. 8. Time evolutions of mixed water mass fractions, $\rho'_2(t)$, in DNS at different resolutions for $Re = 2800$.

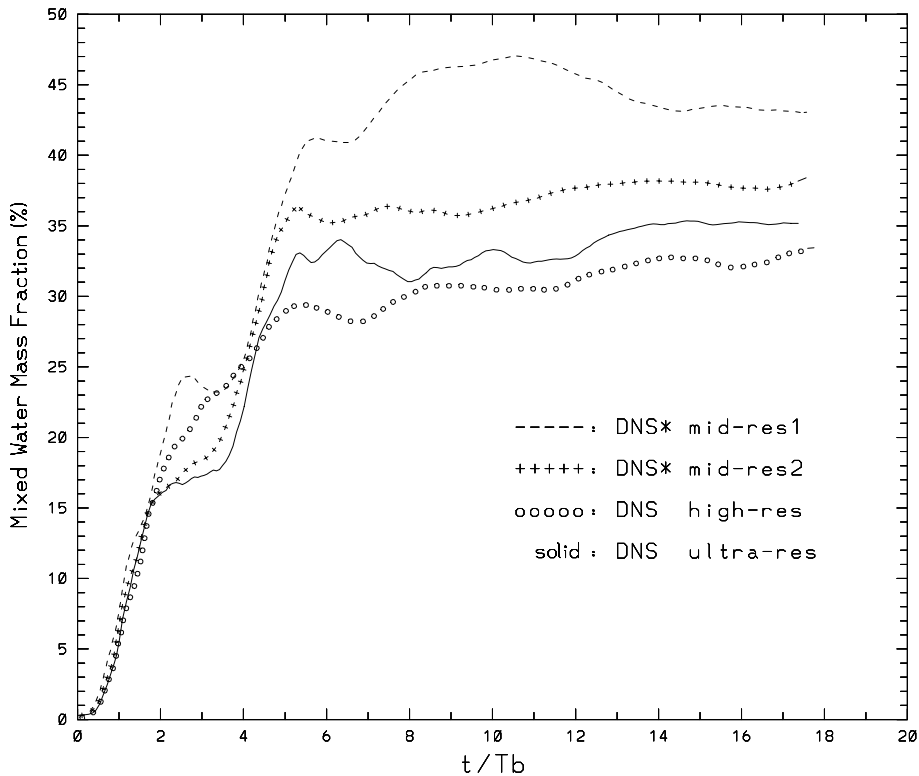


Fig. 9. Time evolutions of mixed water mass fractions, $\rho_2'(t)$, in DNS at different resolutions for $Re = 4300$.

were not successfully completed due to numerical instability that was initiated by jets forming between the initial gravity currents and the side walls at the moment of impact.

5.2. LES results

5.2.1. Comparison of SGS models A–D

LES for the case with $Re = 2800$ are conducted using SGS models A–D with different resolutions listed in Table 1. The results are shown in terms of the volume fraction of water with a density range of $\rho_2'(t)$ in comparison to that from high-res DNS.

Results from classical Smagorinsky SGS, denoted SGS model A, which is extended to apply to the density transport equation, are shown in Fig. 10a. The results at different resolutions exhibit quite a bit of variation about the reference curve, and do not appear to show an improvement with respect to DNS* (Fig. 8). When the vertical turbulent mixing in the density equation is controlled via $f(Ri)$ in SGS model B, LES results at all resolutions are tightly clustered around the curve from high-res DNS. In model C, in which the vertical components of the SGS stresses in only the momentum equations are controlled via $f(Ri)$, the results are significantly worse than both DNS* and other SGS models (Fig. 10c). Finally, when the vertical components of SGS stresses in both momentum and density equations are modulated via $f(Ri)$ in model D, the results are actually quite good, but one case, mid-res2 LES, shows dramatic errors (Fig. 10d).

In conclusion, an improvement with respect to DNS* is found when a simple representation of anisotropic mixing typical of stratified flows is included in the SGS stress in the density equation (models B and D). When this modification, based on the splitting of eddy viscosities into horizontal and vertical components, and regulating the vertical component via $f(Ri)$, is applied only to the momentum equations (model C), the results get worse. In fact, even model D seems to give unexpected behavior, and anisotropic mixing only in the density equation, thus SGS model B, seems to be preferable.

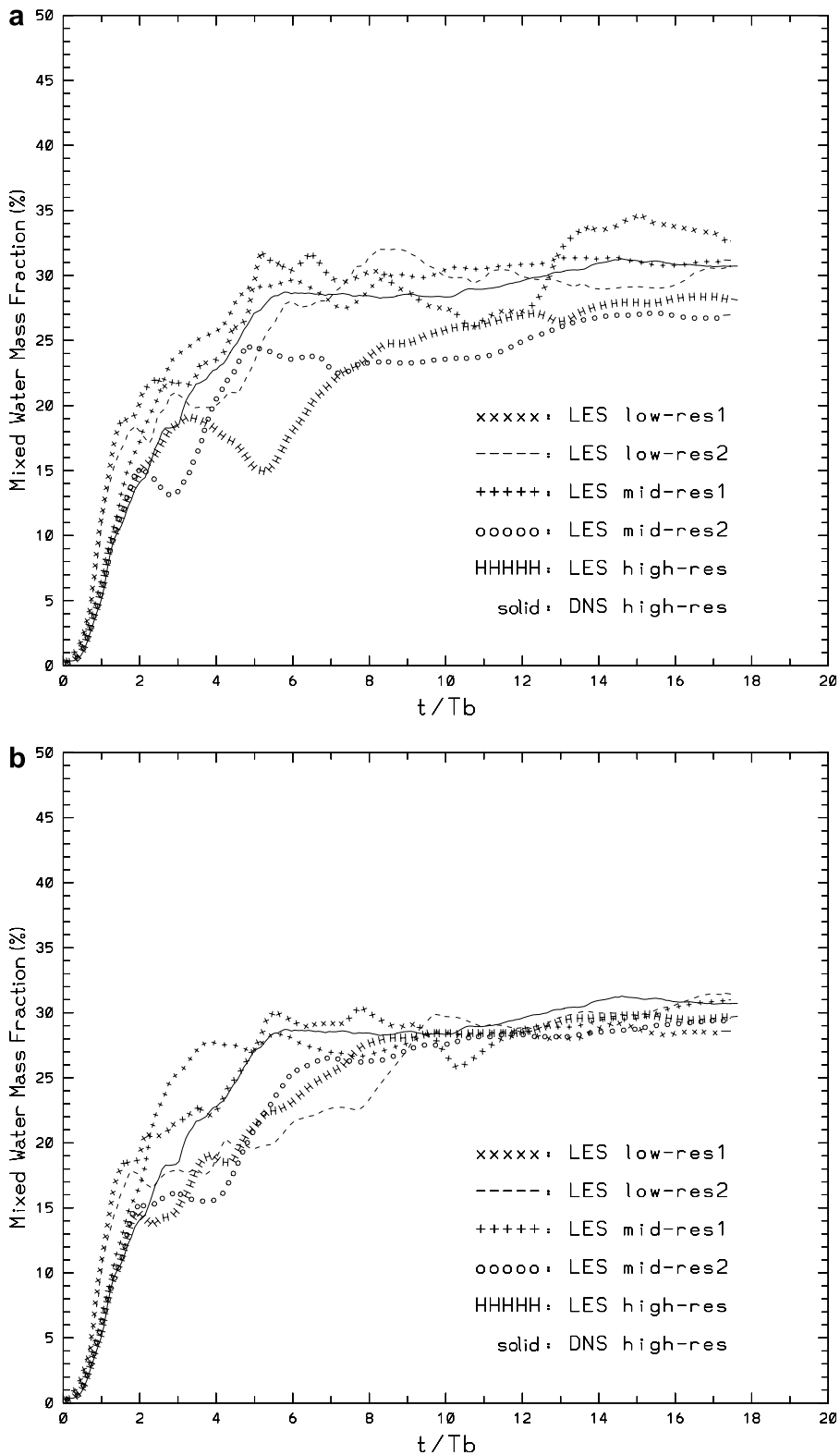


Fig. 10. The time evolutions mixed water mass fraction with $\frac{1}{3} \leq \frac{\rho_2'}{\Delta \rho'} < \frac{2}{3}$ in LES with different resolutions using (a) SGS model A, (b) SGS model B, (c) SGS model C, and (d) SGS model D, in comparison to that from high-res DNS (solid line) for $Re = 2800$. The Smagorinsky constant is $c_s = 0.05$ in all LES experiments.

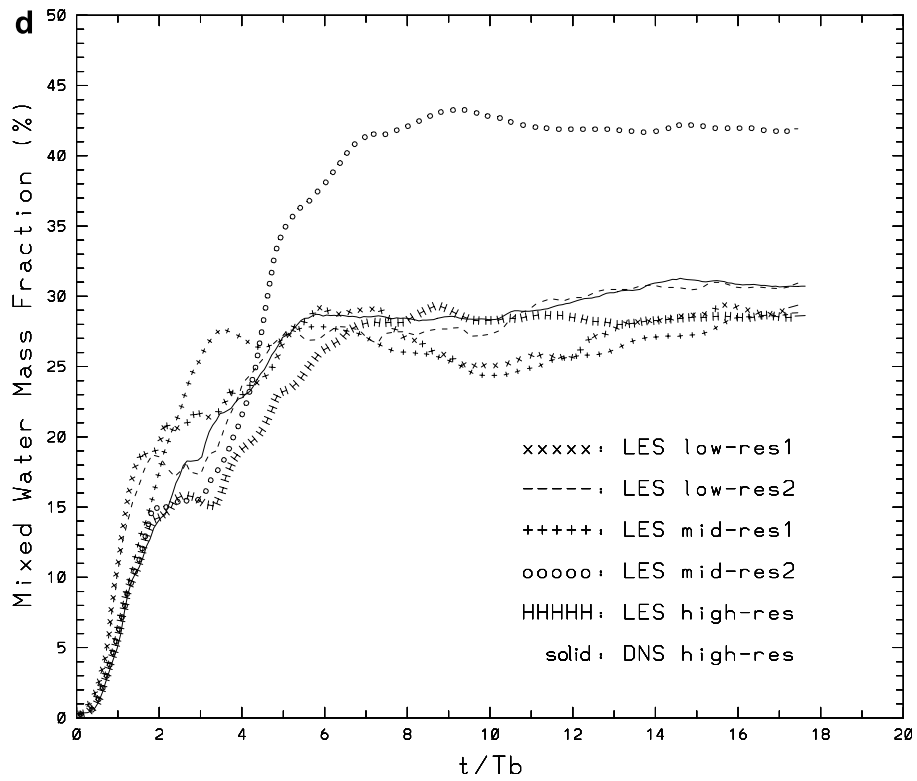
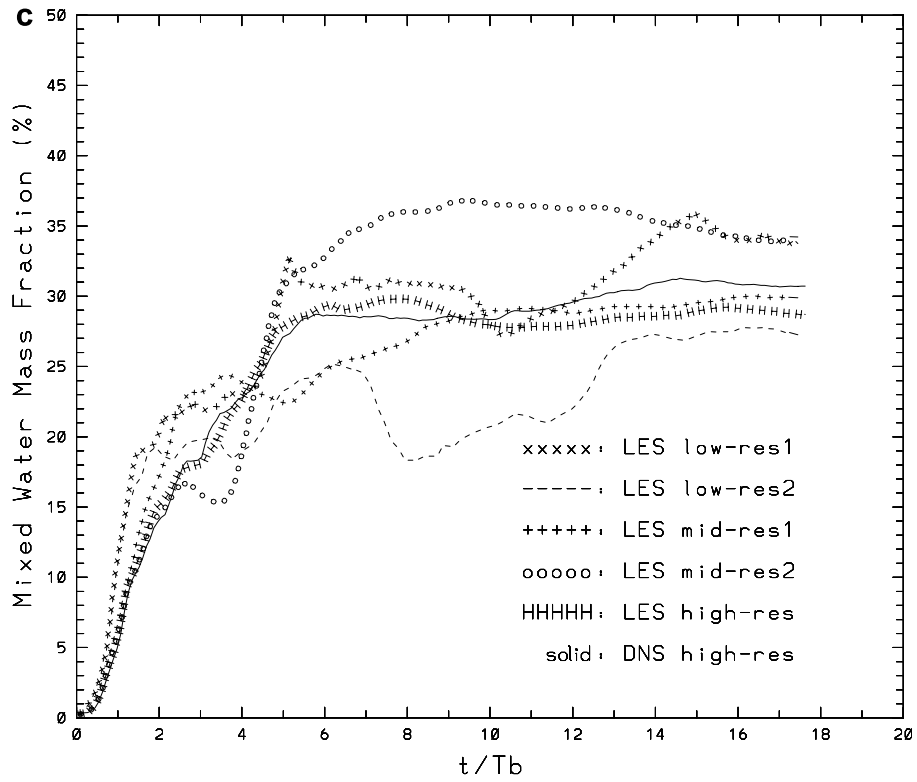


Fig. 10 (continued)

It is worth noting that low-res1 case completed in all LES while it has failed to do so in DNS*. The snapshot of ρ' in low-res1 DNS* just prior to blow up is shown in Fig. 11a, while that of LES with model B is shown in Fig. 11b. Note that all of the numerical noise near the side walls causing numerical instability in DNS* is removed in LES, while the effect of the SGS stress terms on the large-scale density field remains quite small. This is a clear indication that the SGS model provides the dissipation where needed.

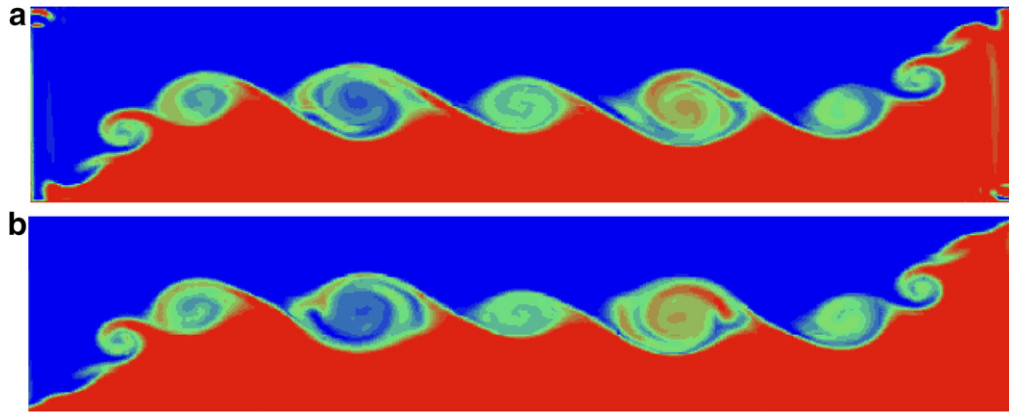


Fig. 11. Snapshots of the density perturbation distribution at $t/T_b = 1.14$ in (a) low-res1 DNS* (just prior to blow up because of numerical instability) and (b) low-res1 LES with SGS model B. Note that most of the numerical noise near the side walls is removed in LES while the effect of the SGS model on the large-scale density field remains very subtle.

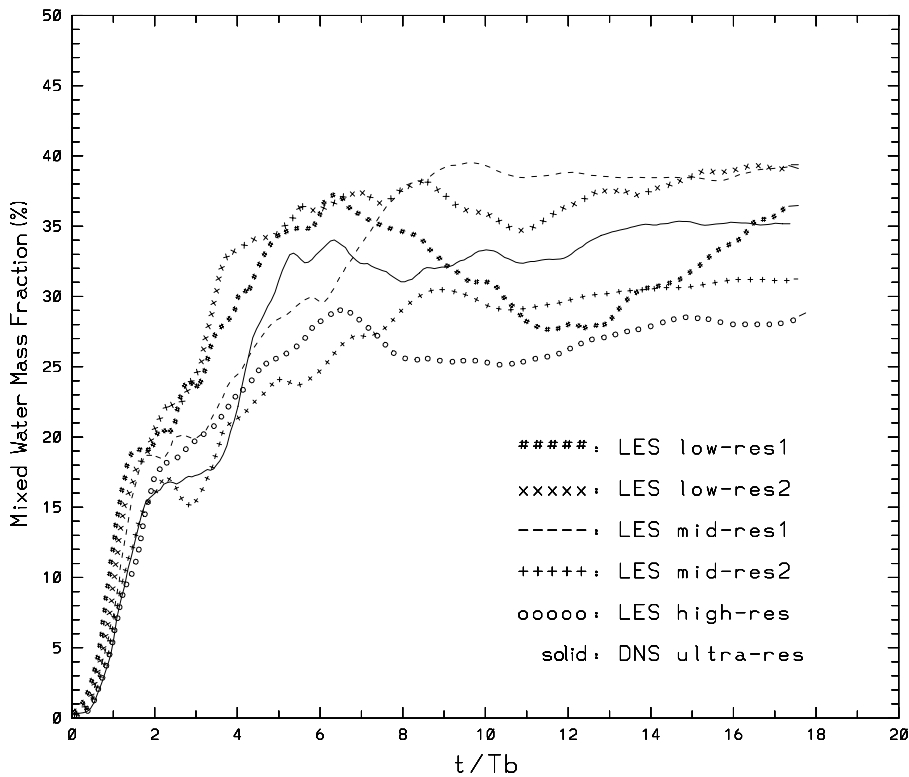


Fig. 12. The time evolutions mixed water mass fraction with $\frac{1}{3} \leq \frac{\rho'_s}{\Delta\rho'} < \frac{2}{3}$ in LES using SGS model B ($c_s = 0.05$) with different resolutions for $Re = 4300$.

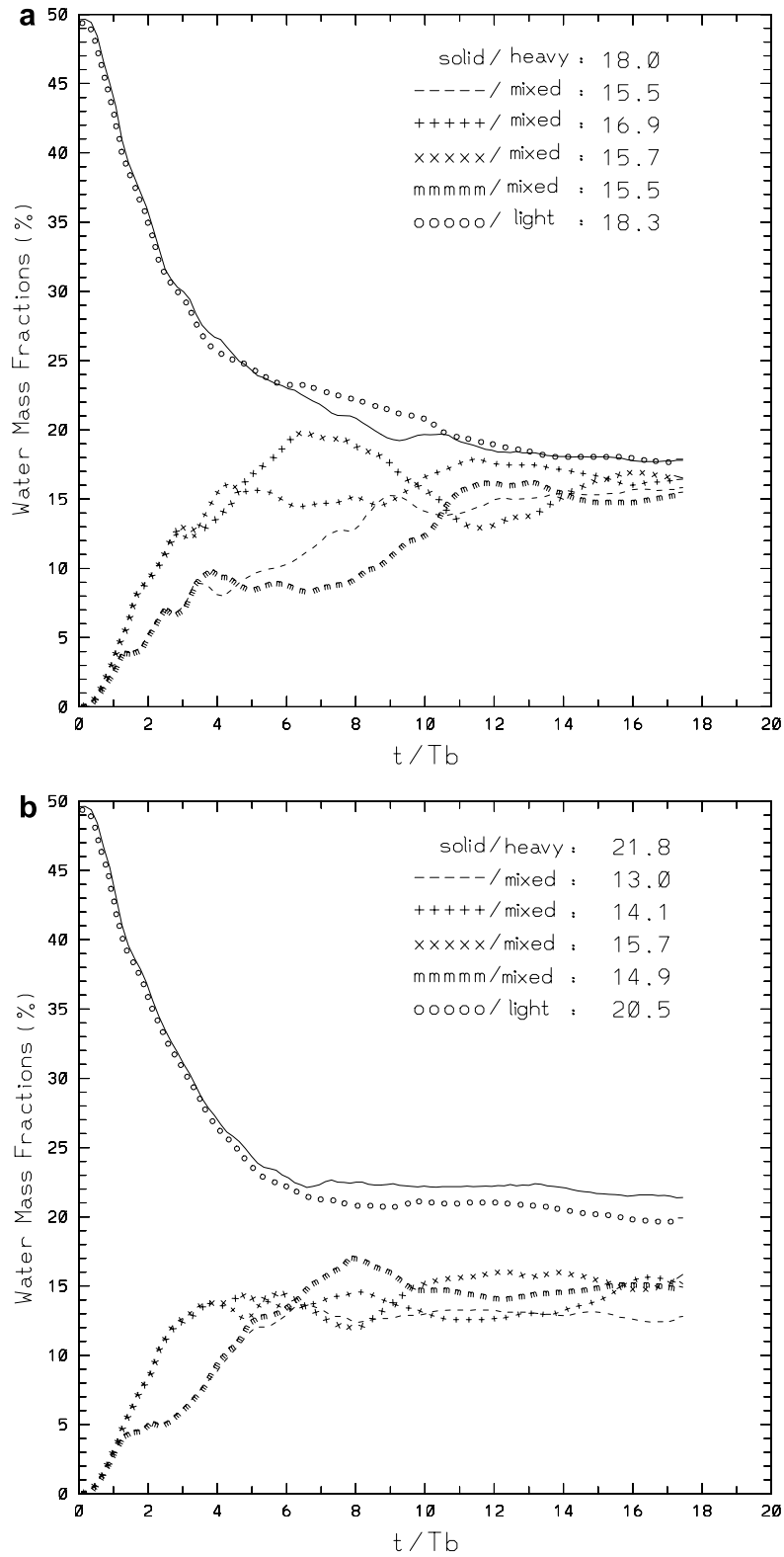


Fig. 13. Time evolutions of water mass fractions (in %) using six segments in (a) mid-res1 DNS* and (b) mid-res1 LES with SGS model B ($c_s = 0.05$) for $Re = 2800$.

LES results using SGS model B with different resolutions for the case of $Re = 4300$ are illustrated in Fig. 12. The LES performance for this case is less impressive than that for $Re = 2800$. Nevertheless, a significant improvement with respect to DNS* (Fig. 9) can be seen for the low resolution cases, namely mid-res1, and of course low-res2 and low-res1 that blew up in DNS* but complete the integration in LES.

Next, we address the question whether using the water mass fraction with density perturbation ρ'_2 can ensure an improved reproduction accuracy of mixing in finer bins as well. The time evolution of mass fractions in six bins in mid-res1 experiments with $Re = 2800$ without (DNS*) and with (LES) SGS model B stress terms are shown in Fig. 13a and b, respectively. Results from DNS* are clearly different from that in the reference experiment (Fig. 7a), in that they do not even reach a statistical steady state, but show a trend, in which fractions of all density bins seem to converge to 1/6. LES results are much more similar to that from high-res DNS, in which there is a clear separation in the steady-state mass fractions of the densest and lightest water masses, and the others. Results from LES with other resolutions demonstrate a similar degree of improvement (not shown). Thus, SGS model B appears to lead to a rectification of the equilibrium p.d.f. of ρ' .

Thus, the above experiments show that LES appears to have a clear advantage in terms of computational cost, i.e. the ability to achieve mixing accuracy when the smallest turbulent coherent structures are under-resolved. The other advantage of LES is presumably to be able to achieve higher Re than possible with DNS given that the smallest dissipative scales do not need to be explicitly resolved. To this end, a higher Re experiment is conducted. A snapshot of the density perturbation distribution in mid-res1 LES with SGS model B at $Re = 9700$ at the instant when the gravity currents reach the side walls is shown in Fig. 14a. The increase in the number of KH rolls indicate a wider range of turbulent scales with respect to the case with $Re = 4300$ (Fig. 14b).

5.2.2. Sensitivity to Smagorinsky coefficient c_s

It is of interest to explore the sensitivity of the results to c_s in order to find out how wide the optimal range is, and how fast the LES performance declines away from the optimal range of the Smagorinsky constant. A mathematical approach to achieve this is via the so-called *continuous sensitivity analysis*, in which the sensitivities of velocity $\partial \bar{\mathbf{u}} / \partial c_s$, pressure $\partial \bar{p} / \partial c_s$, and density perturbation $\partial \bar{\rho}' / \partial c_s$ are approximated by differentiating the Eqs. (12)–(16) with respect to c_s . The resulting equations are linear, and thus they can be solved efficiently. The continuous sensitivity analysis has been used successfully in investigating the sensitivity of fluid flow models with respect to parameters such as geometry, initial conditions, and boundary conditions (Borggaard and Iliescu, 2006; Stanley and Stewart, 2002), and the sensitivity of SGS models with respect to parameters such as c_s (Berselli et al., 2005).

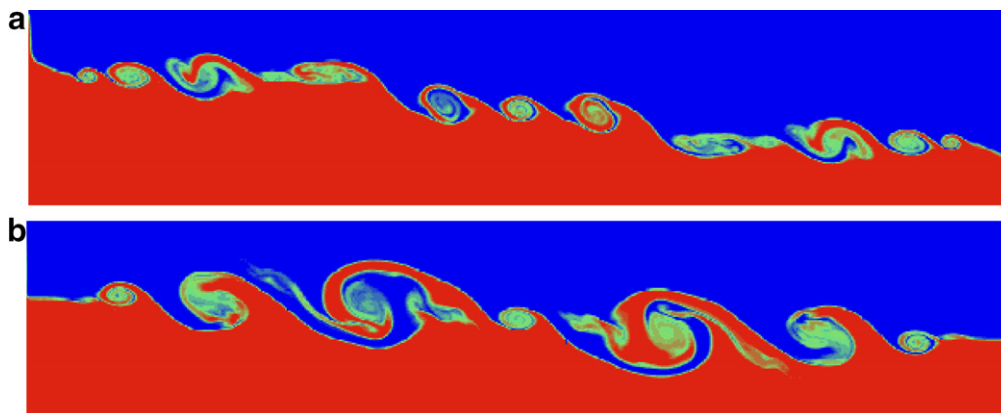


Fig. 14. Snapshots of the density perturbation distribution in mid-res1 LES with SGS model B at (a) $Re = 9700$, and (b) $Re = 4300$ at $t/T_b = 1.9$.

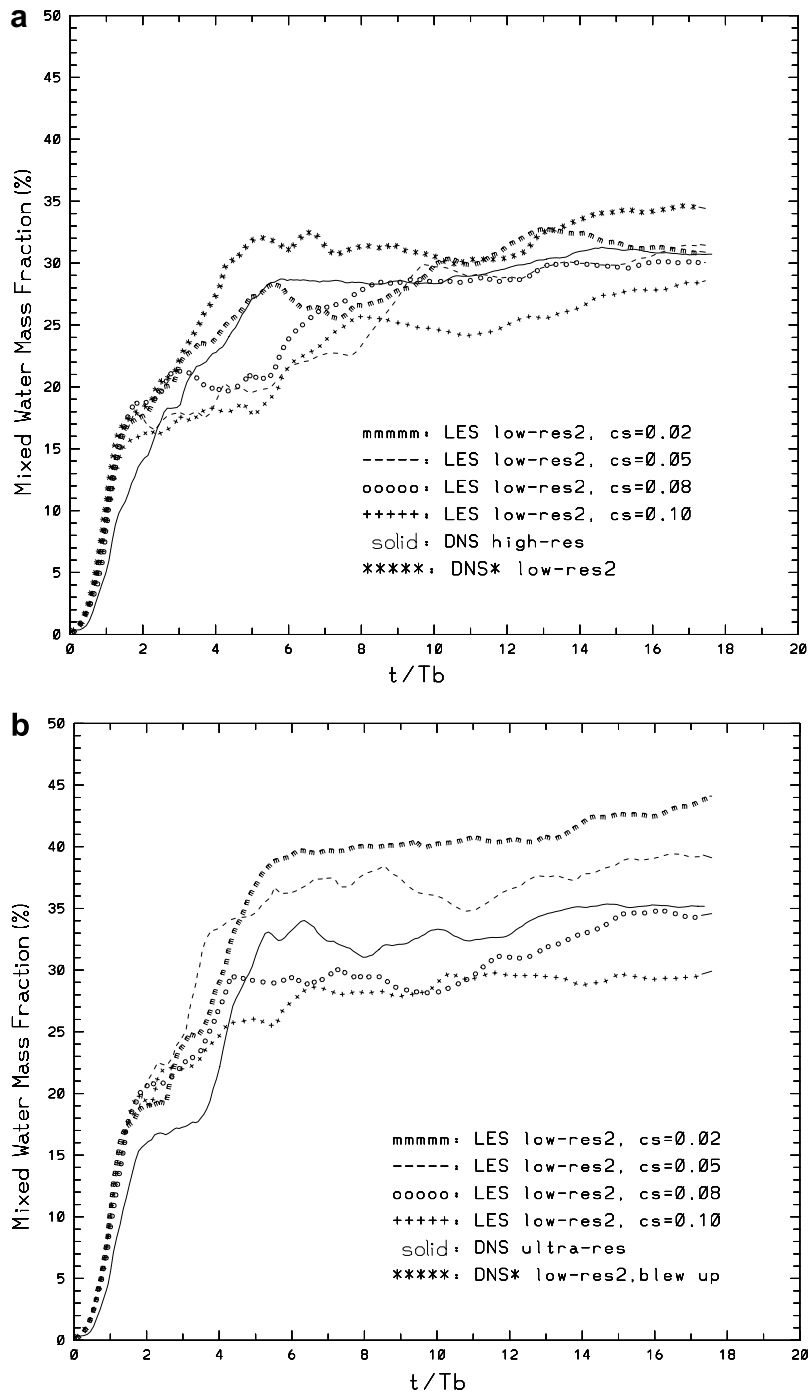


Fig. 15. Sensitivity of the time evolutions mixed water mass fraction with $\frac{1}{3} \leq \frac{\nu_s}{\Delta \rho'} < \frac{2}{3}$ to Smagorinsky coefficients of $c_s = 0.02, 0.05, 0.08, 0.10, 0.15$ in LES with SGS model B in comparison to those from high-res DNS (benchmark curve) and DNS* at the selected resolution (the difference between these lines is a bound for error). Results for (a) low-res2 LES at $Re = 2800$, (b) low-res2 LES at $Re = 4300$, (c) mid-res1 LES at $Re = 4300$.

Here, we follow a simpler approach. LES with model B and several Smagorinsky coefficients of $c_s = 0.02; 0.08; 0.10; 0.15$ are conducted at various resolutions for both $Re = 2800$ and $Re = 4300$. Results

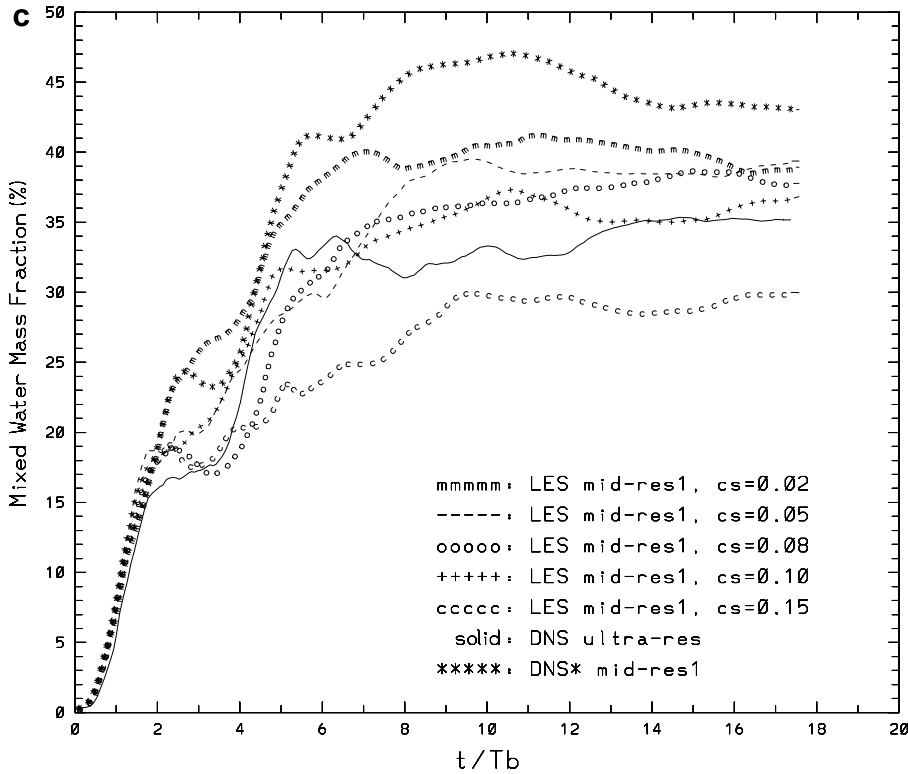


Fig. 15 (continued)

for low-res2 LES at $Re = 2800$, low-res2 LES at $Re = 4300$, and mid-res1 LES at $Re = 4300$ are shown in Fig. 15a–c, respectively. In addition to the benchmark results of high-res and ultra-res DNS, the corresponding curves from low-res2 and mid-res1 DNS* are included in each case, as the difference between DNS and DNS* is a bound for error to evaluate the optimal range for c_s . All LES seem to show an improvement with respect to equal-resolution DNS*, which indicates that the LES performance is not related to a specific value of $c_s = 0.05$, but smoothly varies with c_s spanning almost an order of magnitude. However, the case with $c_s = 0.02$ approaches DNS*, and it may not provide adequate dissipation where needed. On the other hand, the case with $c_s = 0.15$ (only mid-res1 LES is shown) is too diffusive, significantly modifying the large-scale density field with respect to DNS*. The difference in behavior between $Re = 2800$ and $Re = 4300$ may be indicative that optimally $c_s = c_s(Re)$, but this issue is not further pursued here given the limited range of Re achievable in DNS with the computational resources available to us at the present time. Overall, a range of $0.05 \leq c_s \leq 0.10$ seems to be preferable based on these results, with the desirable properties of LES, namely adequate dissipation where needed and a subtle modification of the large-scale flow and density fields, declining gradually beyond this range.

5.2.3. Sensitivity to vertical mixing curve $f(Ri)$

We explore the sensitivity of the time evolutions mixed water mass fraction with $\frac{1}{3} \leq \frac{\rho'_2}{\Delta\rho'} < \frac{2}{3}$ to changes in the vertical mixing coefficient curve (17). In particular, the following functions are tested (although other choices exist)

$$f(Ri) = 1 - \frac{Ri}{Ri_c} \quad \text{and} \quad f(Ri) = \left(1 - \frac{Ri}{Ri_c}\right)^2 \quad \text{for } 0 \leq Ri \leq Ri_c, \quad (39)$$

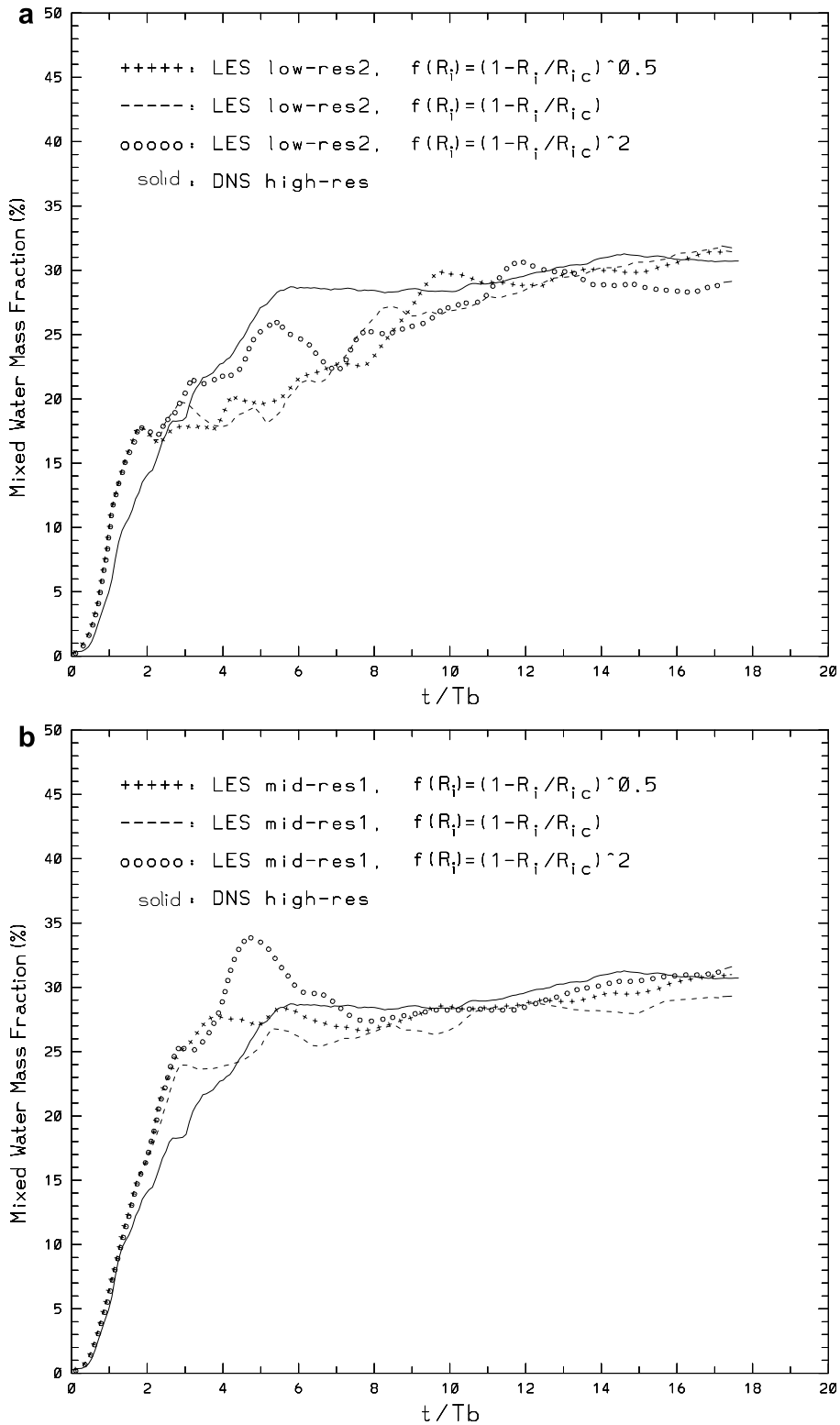


Fig. 16. Sensitivity of the time evolutions mixed water mass fraction with $\frac{1}{3} \leq \frac{\nu_s'}{\Delta\rho'} < \frac{2}{3}$ to changes in the mixing curve for (a) low-res2 LES, and (b) mid-res1 LES at $Re = 2800$. Solid line denotes high-res DNS, lines with “+” the LES results with the original $f(Ri) = \sqrt{1 - \frac{Ri}{Ri_c}}$ for $0 \leq Ri \leq Ri_c$, lines with “-” the LES results with a modified mixing curve $f(Ri) = 1 - \frac{Ri}{Ri_c}$, and lines with “o” the results with $f(Ri) = \left(1 - \frac{Ri}{Ri_c}\right)^2$.

that correspond to small differences from the original curve (Fig. 1). LES are conducted for two resolutions low-res2 and mid-res1 at $Re = 2800$ using $c_s = 0.05$ and SGS model B. Results shown in Fig. 16a and b indicate that the differences from $f(Ri) = \sqrt{1 - \frac{Ri}{Ri_c}}$ appear to be very small for cases with $f(Ri) = 1 - \frac{Ri}{Ri_c}$, whereas they are somewhat larger for cases with $f(Ri) = (1 - \frac{Ri}{Ri_c})^2$. In the latter case $df(Ri)/dRi$ near $Ri \approx Ri_c$ is quite small and acts to reduce the effective value of Ri_c .

5.2.4. Sensitivity to resolution of overturning scales

It is shown above that the SGS model B provides subtle corrections to the resolved flow field, which, in the absence of this SGS model, gradually diverges from the reference mixing characteristics as the resolved scales become coarser. The following question then arises: *What is the coarsest resolution one can use before LES becomes ineffective, or in other words, what is the upper limit for the cutoff scale δ ?*

The main underlying concept of LES is the computation of the large eddies that provide most of the mixing, and parameterization of the small eddies that dissipate the energy cascading from the larger scales. Thus, in effect, the question is what is the energy-containing scale in this stratified mixing problem.

Gargett et al. (1984) have shown that the energy-containing scale in stratified mixing problem is set by the Ozmidov scale ℓ_O and provided that ℓ_O is much larger than the dissipation (Kolmogorov) scale, the energy spectrum between these two scales tends to approach one in K-41 theory, with smaller scales becoming increasingly more isotropic. This implies that the filter scale δ must be small enough to resolve ℓ_O for LES to be effective.

The Ozmidov scale is defined as $\ell_O = \sqrt{\epsilon/N^3}$, where ϵ is the turbulent kinetic energy dissipation rate and N is the buoyancy frequency. By dimensional arguments (Taylor, 1935; Pope, 2000), ϵ can be estimated from $\epsilon = c_\epsilon u_0^3/h_0$, where u_0 is a characteristic velocity of energy-containing turbulent eddies, h_0 is their characteristic length scale, and c_ϵ is a proportionality constant. While this scaling was originally introduced for homogeneous fluids, it is expected to hold for stratified fluids as well (Gargett, 1994) by setting $h_0 \approx \ell_O$. The characteristic eddy velocity u_0 is assumed to be equal to the initial propagation speed of the gravity currents $u_0 \approx U_0 = \frac{1}{2}\sqrt{g\Delta\rho'H/\rho_0}$. The buoyancy frequency N becomes $N = \sqrt{-\frac{g}{\rho_0}\frac{\partial\rho'}{\partial z}} \approx \sqrt{\frac{g}{\rho_0}\frac{\Delta\rho'}{\ell_0}}$. The estimates for c_ϵ from oceanic, atmospheric and laboratory measurements vary over a wide range of 0.04–5 (Kantha and Clayson, 2000) but $0.6 \leq c_\epsilon \leq 0.8$ is most common (Moum, 1996). Taking $c_\epsilon \approx 0.7$ we obtain for the initial overturning scales

$$\frac{\ell_O}{H} \approx 0.25c_\epsilon^{2/3} \approx 0.2. \quad (40)$$

This can be confirmed visually from the scales of Kelvin–Helmholtz rolls in Fig. 2b and c.

All LES with higher or equal resolution than mid-res1 look visually similar to DNS fields shown in Fig. 2. The lowest resolution LES conducted so far, low-res1 has smoother fields, but the main overturning scale is still well resolved (Fig. 11b vs Fig. 2c). Next, we conduct experiments by gradually reducing the resolution, namely by placing the filter scale at larger scales, to investigate when and how LES fails. The detail of these

Table 2
Table of the numerical experiments with coarse resolution

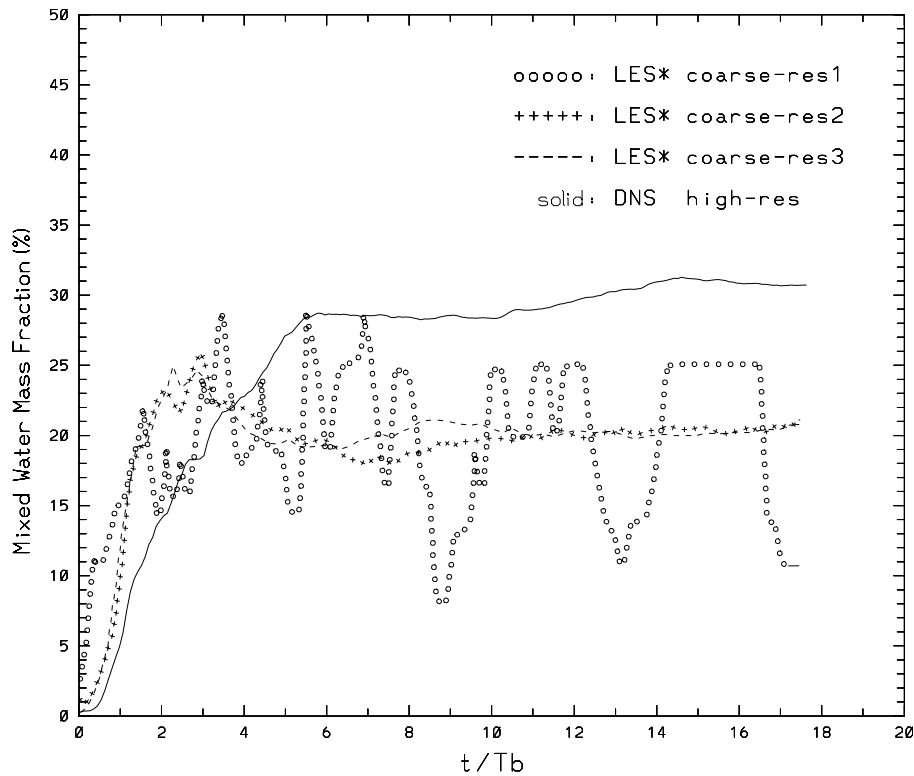
Resolution	$Re = 2800, Pr = 7$
coarse-res1 $K = 2; N = 6; 72$ points	LES*
coarse-res2 $K = 75; N = 6; 2700$ points	LES*
coarse-res3 $K = 176; N = 6; 6336$ points	LES*

LES* denotes under-resolved simulations with the SGS stress model.

Table 3

The ratio of the filter scale δ to domain height H and to the initial Ozmidov scale ℓ_O in all LES

Resolution	δ/H	ℓ_O/δ
high-res LES	0.0065	30.8
mid-res2 LES	0.0080	25.0
mid-res1 LES	0.0117	17.1
low-res2 LES	0.0302	6.6
low-res1 LES	0.0368	5.4
coarse-res3 LES*	0.0395	5.1
coarse-res2 LES*	0.0606	3.3
coarse-res1 LES*	0.3690	0.5

Fig. 17. The time evolutions mixed water mass fraction with $\frac{1}{3} \leq \frac{\rho'_2}{\Delta \rho'} < \frac{2}{3}$ in LES* using SGS model B ($c_s = 0.05$) with different resolutions.

experiments, referred to as coarse-res1 to coarse-res3, is given in Table 2, and denoted as LES* as (shown below) the overturning scales are under-resolved in these cases.

The filter scale is $\delta = \sqrt{\Delta x_{\max} \Delta z_{\max}}$ where Δx_{\max} and Δz_{\max} are the maximum distances between Lagrange polynomial points in the spectral element discretization. The ratios of the filter scale to domain height δ/H and to the initial Ozmidov scale ℓ_O/δ for all resolutions are tabulated in Table 3.

The time evolutions mixed water mass fraction with $\frac{1}{3} \leq \frac{\rho'_2}{\Delta \rho'} < \frac{2}{3}$ in LES* using SGS model B ($c_s = 0.05$) are shown in Fig. 17, which indicates that coarse-res3 LES* and coarse-res2 LES* do reasonably well until about $t/T_b \approx 4$, after which they lead to an underestimate of the mixing, whereas coarse-res1 LES* leads to erratic results. The reasons can be identified from the snapshots of density perturbations in the experiments. In coarse-res2 LES* (similar result is obtained for coarse-res3 LES*) the initial overturning scales are reasonably well captured despite significant phase and growth rate errors (Fig. 18a vs Fig. 2c), while the fine-scale

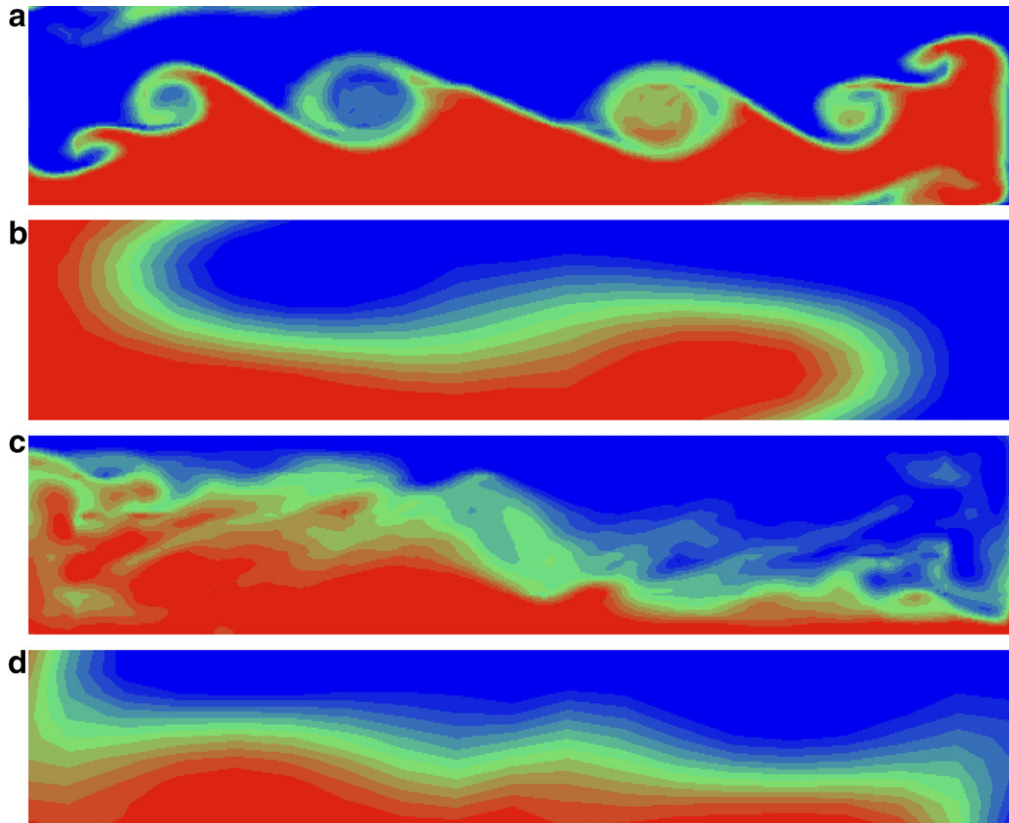


Fig. 18. Distribution of the density perturbation for (a) coarse-res2 LES* $t/T_b = 1.17$, (b) coarse-res1 LES* $t/T_b = 1.17$, (c) coarse-res2 LES* $t/T_b = 4.00$, (d) coarse-res1 LES* $t/T_b = 4.00$.

filaments and smaller overturning eddies appearing later in the experiment are mostly missing (Fig. 18c vs Fig. 2d), leading to a saturation of mixing and significant errors (about 33% underestimate of the total mixed water fraction) later in the experiment. The overturning scales are not resolved in coarse-res1 LES* (Fig. 18b and d).

More quantitatively, turbulent overturning scales are computed using Thorpe's (Thorpe, 1977) method. This method consists of reordering a model/data density profile, which may contain inversions, into a stable monotonic profile that contains no inversions. Thorpe displacement d is the distance that the water parcel must travel vertically in order to reach neutral buoyancy. The overturning scale ℓ_T is defined as the rms of the displacements, $\ell_T = \langle d^2 \rangle^{1/2}$ for $d \neq 0$. Then domain-averaged Thorpe scale $\overline{\ell_T}(t) = L^{-1} \int_0^L \ell_T(t, x') dx'$ is calculated. The average overturning scales in the domain $\overline{\ell_T}(t)$ are plotted for selected experiments in Fig. 19. Overturning scales ℓ_T grow by the shear induced by counter-propagating gravity currents initially and they are periodically regenerated by the back and forth slushing in the computational domain ($\overline{\ell_T}$ for high-res DNS). However, after every cycle, there is a slight reduction in the size of the smallest $\overline{\ell_T}$ because mixing events reduce the density gradients, which reduces the vertical shear, which in turn reduces generation of turbulent kinetic energy during the period when the flow propagates between the walls. In low-res2 LES, $\overline{\ell_T}(t)$ is quite well captured. In all higher resolution LES, time evolutions of $\overline{\ell_T}(t)$ are very close to that from high-res DNS (not shown). While the first two cycles are well captured in coarse-res2 LES, at $t/T_b \approx 5$ the Nyquist rule $\overline{\ell_T}/\delta \geq 2$ appears to be violated and the overturning scales are missed during the rest of the simulation, leading to the underestimation of mixing seen in Fig. 17. None of the overturning scales are resolved in coarse-res2 LES* and the concept of LES fails entirely.

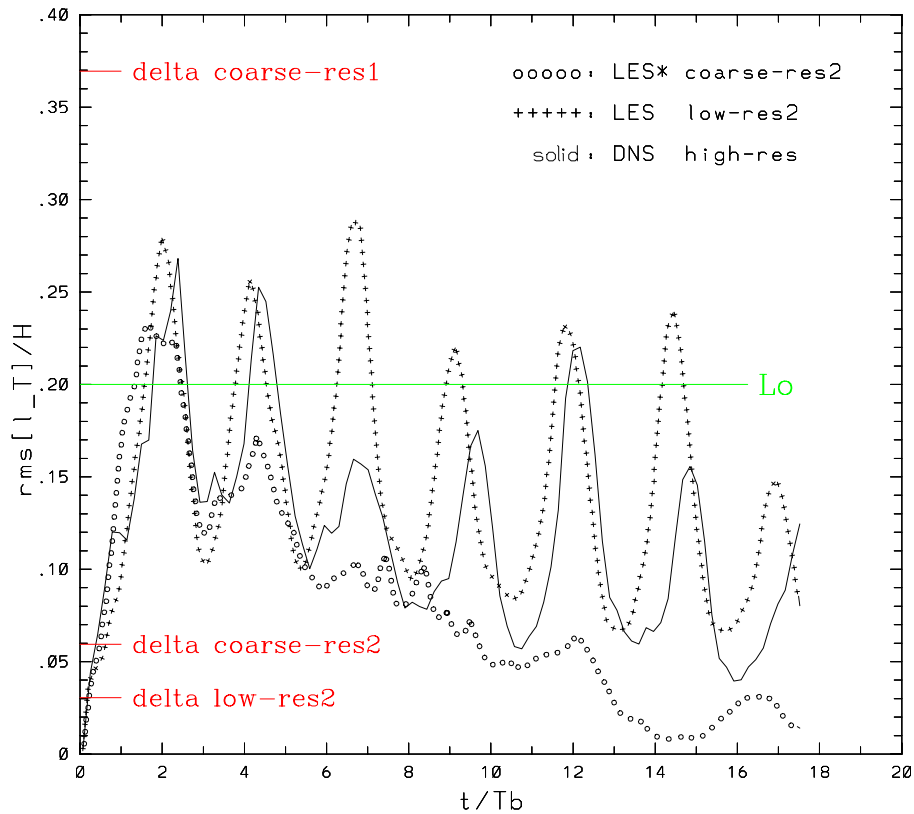


Fig. 19. Time evolutions of the average turbulent overturning scale $\overline{\ell_T}/H$ in high-res DNS, low-res2 LES and coarse-res2 LES*. The green line marks the initial Ozmidov scale ℓ_O from (40). The red lines mark filter scales δ/H from low-res2 LES, coarse-res2 LES* and coarse-res1 LES*.

6. Summary and conclusions

Stratified mixing plays an important role in the coastal ocean circulation by affecting the transport of pollutants, sediments and biological species, as well as globally by determining the nature of the thermohaline circulation. Observations are essential to improve our understanding of this phenomenon. However, observations alone are not sufficient since such mixing takes place over large distances and/or in deep ocean, such that the present-day observational techniques relying on one-dimensional or Lagrangian measurements typically undersample the turbulent flow field in space and time coordinates. Most ocean general circulation or coastal models are based on the hydrostatic approximation, which is not valid for the dynamics of such mixing. Therefore, it seems timely and necessary to employ a new class of nonhydrostatic models that would complement interpretation and further exploration of the dynamical picture emerging from observations, and could be used to develop parameterizations of subgrid-scale processes for basin and global-scale ocean models. In this sense, LES is a relatively new technique in ocean modeling that can be useful to address a wide range of important problems.

However, SGS models for LES have been developed primarily in the engineering community for homogeneous fluid flows, and the applicability of such models to stratified flows has not been investigated exhaustively. The objective of the present study is to explore how LES, with several SGS models based on Smagorinsky eddy viscosity and diffusivity, would perform in a basic stratified mixing problem. To this end, the dam-break problem in a rectangular enclosed domain is selected as the testbed. While this problem offers a number of simplifications regarding the initial conditions, boundary conditions and geometry, which by themselves contain separate and challenging issues in the context of filtering for LES, it is also dynamically demanding, showing a gradual transition from shear-induced mixing to a regime in which a complex

interaction between shear instability and internal waves takes place. In particular, as only two density classes exist at the initial state, the exact volume fraction of intermediate density classes depends on the details of mixing between these two water masses, and this forms a reliable criterion to assess the performance of LES.

To investigate this issue, 2D numerical experiments with two different sets of physical parameters, $Re = 2800$ and $Re = 4300$, both with $Pr = 7$ and $Fr = 2^{-\frac{1}{2}}$, are conducted in a rectangular domain with an aspect ratio of $a = 5$, which is enclosed via insulation, no through-flow, and free-slip boundary conditions. The numerical model is a nonhydrostatic spectral element model Nek5000, which exhibits minimal numerical dissipation and dispersion errors, allowing a reliable investigation of the effect of the SGS models on the system. First, experiments are conducted without SGS models by varying the spatial resolutions. The highest resolution experiments (DNS) are denoted high-res and ultra-res and they constitute the benchmark for this selection of parameters. Under-resolved simulations, so-called DNS*, allow us to determine the impact of SGS terms that are included in the case of LES. Four versions of the Smagorinsky SGS model are tested. Model A is the classic Smagorinsky model extended also to the density transport equation. In model B, the vertical component of eddy diffusion is modulated via a function $f(Ri)$, such that the vertical diffusion coefficient gradually reduces to zero for $0 \leq Ri < Ri_c$ with $Ri_c = 1/4$, and it is zero for $Ri \geq Ri_c$, to incorporate the anisotropic mixing characteristic in stratified flows (e.g., Fernando, 2000; Rohr et al., 1988; Miles, 1961). In model C, such $f(Ri)$ is used in the momentum equations rather than the density equation, whereas in model D, it is incorporated in all momentum and density conservation equations. The LES performance is assessed by monitoring the p.d.f. of ρ' , or more specifically, by using the time evolution of the volume fraction of intermediate density water masses generated by mixing.

It is found that all tested SGS models lead to improved results with respect to those from DNS*, but model B shows the most faithful reproduction of mixed water masses at all resolution tested, and also allows for simulations with low resolution cases low-res1 and low-res2, which blow up in DNS* due to lack of adequate dissipation where needed. In contrast, model C gives the worst results, even worse than model A that does not include Ri -modulated control of vertical mixing. These results indicate that not all Ri -dependent SGS models work equally well and care is needed in incorporating them.

The results also illustrate a significant computational advantage of the SGS model B in reproducing reasonably accurately the bulk mixing characteristics in this system at coarse resolution. Once the dynamical accuracy of this SGS model is validated, LES with $Re = 9700$ is conducted at mid-res1, the DNS of which is computationally prohibitive at this particular resolution. The objective here is to highlight the dual computational advantage of LES for problems relevant to ocean circulation: Given a numerical mesh, LES can produce accurate results for Re for which DNS* (i.e., under-resolved simulations without any SGS model on the same numerical mesh) either gives inaccurate results, or simply blows up. Alternatively, given a Re , LES can yield accurate results at a fraction of the computational cost (i.e. number of meshpoints) required by a DNS to achieve the same accuracy. For instance in this study, the computational cost of low-res1 LES is approximately 1000-fold less than that for ultra-res DNS.

Since the SGS model has a tunable parameter c_s , sensitivity experiments are conducted, which demonstrate that optimal results are obtained in the range of $0.05 \leq c_s \leq 0.10$. For $c_s < 0.05$ the dissipation provided by the SGS model may not be adequate, and for $c_s > 0.10$, the SGS model may supply too much dissipation, reducing the shear and density gradients in the large-scale flow, which then alters the mixing characteristics. This range of c_s is generally consistent with what is found to be optimal for LES of homogeneous shear flows. The results are found to be robust also to small changes in $f(Ri)$. Experiments with coarse resolution indicate that the average overturning scale ℓ_O must be resolved for LES to be effective. For cases of $\delta > \ell_O$, more classical techniques such as RANS relying on full prognostic equations for turbulent kinetic energy and dissipation (or other quantities) are likely to be more effective, since SGS models for LES are usually dynamically simple.

Much remains to be done regarding the adaptation of LES as a tool to study ocean flows. First, the tunable constant c_s may be different in 2D and 3D flows, since the characteristics of turbulence are different, and it may also be a function of Re . To this end, *dynamic* models, in which the flow field is filtered at two different scales to allow for the estimation of $c_s(\mathbf{x}, t)$, need to be explored for stratified flows. Second, the down-scale transfer of energy as implied by EV models is valid only in the statistical sense, and such models do not allow for so-called backscatter which is significant in transitional flows and due to 2D phenomena such as vortex pairing. Other types of SGS models need to be investigated. Third, the treatment of the boundary conditions in the

presence of solid boundaries (discussed in detail in Section 4) and complex geometries needs to be brought up to a level to include the progress achieved in the engineering community. Fourth, the continuous sensitivity approach could yield a more reliable estimation of the sensitivity of SGS models with respect to different parameters (such as c_s) in stratified flows. We plan to address these issues in future studies.

Acknowledgments

We greatly appreciate the support of National Science Foundation via grants OCE 0336799, OCE 0352047, DMS 0209326, DMS 0209309, DMS 0322852, and DMS 0513542, the Air Force Office of Scientific Research grants F49620-03-1-0243 and FA9550-05-1-0449, and the Mathematical, Information, and Computational Sciences Division subprogram of the Office of Advanced Scientific Computing Research, US Department of Energy, under Contract W-31-109-ENG-38. We thank Hartmut Peters, Mohamed Iskandarani, Marcello Magaldi and Mehmet Ilicak for valuable comments. We also thank the three anonymous reviewers for their constructive comments, which helped greatly improve the manuscript.

References

- Aldama, A., 1990. Filtering techniques for turbulent flow simulation. Springer Lecture Notes in Engineering, vol. 56. Springer, Berlin.
- Baumert, H., Peters, H., 2004. Turbulence closure, steady state, and collapse into waves. *J. Phys. Oceanogr.* 34, 505–512.
- Berselli, L., Iliescu, T., Layton, W., 2005. Mathematics of Large Eddy Simulation of Turbulent Flows. Springer Verlag.
- Boegman, L., Imberger, J., Ivey, J.N., Antenucci, J.P., 2003. High frequency internal waves in large stratified lakes. *Limnol. Oceanogr.* 48 (2), 895–919.
- Borggaard, J., Iliescu, T., 2006. Approximate deconvolution boundary conditions for LES. *Appl. Math. Lett.* 19 (8), 735–740.
- Borggaard, J., Burkardt, J., Gunzburger, M. (Eds.), 1995. Optimal design and control. Progress in Systems and Control Theory, vol. 19. Birkhäuser Boston Inc., Boston, MA, ISBN 0-8176-3808-3.
- Bourgault, D., Kelly, D.E., 2003. Wave-induced boundary mixing in a partially mixed estuary. *J. Mar. Res.* 51, 553–576.
- Buffett, B.A., 2003. A comparison of subgrid-scale models for large-eddy simulations of convection in the earth's core. *Geophys. J. Int.* 153, 753–765.
- Chang, Y., Xu, X., Özgökmen, T., Chassignet, E., Peters, H., Fischer, P., 2005. Comparison of gravity current mixing parameterizations and calibration using a high-resolution 3d nonhydrostatic spectral element model. *Ocean Modell.* 10, 342–368.
- Chapman, D., 1979. Computational aerodynamics, development and outlook. *AIAA J.* 17, 1293–1313.
- Das, A., Moser, R., 2001. Filtering boundary conditions for LES and embedded boundary simulations. In: Liu, C., Sakell, L., Beutner, T. (Eds.), DNS/LES Progress and Challenges. Greyden Press, Columbus, pp. 389–396.
- Deardorff, J.W., 1974. Three-dimensional numerical study of turbulence in an entraining mixed layer. *Boundary-Layer Meteorol.* 7, 199–226.
- Deardorff, J.W., 1980. Stratocumulus-capped mixed layers derived from a three-dimensional model. *Boundary-Layer Meteorol.* 80, 495–527.
- Doglioli, A.M., Griffa, A., Magaldi, M.G., 2004. Numerical study of a coastal current on a steep slope in presence of a cape: the case of the promontorio di portofino. *J. Geophys. Res.* 109. doi:10.1029/2004JC002422.
- Dörnbrack, A., 1998. Turbulent mixing by breaking gravity waves. *J. Fluid Mech.* 375, 113–141.
- Dryja, M., Widlund, O.B., 1987. An additive variant of the schwarz alternating method for the case of many subregions. Technical Report 339, Department of Computer Science, Courant Institute.
- Dunca, A., John, V., Layton, W., 2004. The commutation error of the space averaged Navier–Stokes equations on a bounded domain. In: Contributions to Current Challenges in Mathematical Fluid Mechanics. Adv. Math. Fluid Mech. Birkhäuser, Basel, pp. 53–78.
- Farmer, R., Pawlowicz, D., Jiang, R., 2002. Tilting separation flows: a mechanism for intense vertical mixing in the coastal ocean. *Dyn. Atmos. Oceans* 36, 43–58.
- Fernando, H.J.S., 2000. Aspects of stratified turbulence. In: Kerr, R.M., Kimura, Y. (Eds.), Developments in Geophysical Turbulence. Kluwer, pp. 81–92.
- Ferziger, J., 2005. Direct and large-eddy simulation of turbulence. In: Baumert, H.Z., Simpson, J.H., Sündermann, J. (Eds.), Marine Turbulence – Theories, Observations and Models. Cambridge University Press, pp. 160–181.
- Fischer, P.F., 1997. An overlapping schwarz method for spectral element solution of the incompressible Navier–Stokes equations. *J. Comput. Phys.* 133, 84–101.
- Fischer, P.F., Mullen, J.S., 2001. Filter-based stabilization of spectral element methods. *Comptes rendus de l'Académie des sciences Paris, – Série I – Analyse numérique* 332, 265–270.
- Fischer, P.F., Miller, N.I., Tufo, H.M., 2000. An overlapping schwarz method for spectral element simulation of three-dimensional incompressible flows. In: Luskin, P.B.M. (Ed.), Parallel Solution of Partial Differential Equations. Springer-Verlag, pp. 159–181.
- Frisch, U., 1995. Turbulence, The Legacy of A.N. Kolmogorov. Cambridge University Press, Cambridge.
- Fureby, C., Tabor, G., 1997. Mathematical and physical constraints on large-eddy simulations. *Theor. Comput. Fluid Dyn.* 9, 85–102.

- Gargett, A., 1994. Observing turbulence with a modified acoustic doppler profiler. *J. Atmos. Ocean. Technol.* 11, 1592–1610.
- Gargett, A., Osborn, T., Nasmyth, P., 1984. Local isotropy and the decay of turbulence in a stratified fluid. *J. Fluid Mech.* 144, 231–280.
- Germano, M., Piomelli, U., Moin, P., Cabot, W., 1991. A dynamic subgrid-scale eddy viscosity model. *Phys. Fluids A* 3, 1760–1765.
- Geyer, W.R., 1993. Three-dimensional tidal flow around headlands. *J. Geophys. Res.* 98 (C3), 3189–3197.
- Gibson, C., Nabatov, V., Ozmidov, R., 1993. Measurements of turbulence and fustil turbulence near ampere seamount. *Dyn. Atmos. Oceans* 19, 175–204.
- Gill, A.E., 1982. *Atmosphere–Ocean Dynamics*. Academic Press, New York.
- Hölmboe, J., 1962. On the behavior of symmetric waves in stratified shear layers. *Geophys. Publ.* 24, 67–72.
- Horn, D.A., Imberger, J., Ivey, G.N., 2001. The degeneration of large-scale interfacial gravity waves in lakes. *J. Fluid Mech.* 434, 181–207.
- Iliescu, T., Fischer, P.F., 2003. Large eddy simulation of turbulent channel flows by the rational LES model. *Phys. Fluids* 15, 3036–3047.
- Iliescu, T., Fischer, P.F., 2004. Backscatter in the rational LES model. *Comput. Fluids* 33, 783–790.
- Kaltenbach, H.J., Gerz, T., Schumann, U., 1994. Large-eddy simulation of homogeneous turbulence and diffusion in stably stratified shear flow. *J. Fluid Mech.* 280, 1–40.
- Kantha, L.H., Clayson, C.A., 2000. *Small Scale Processes in Geophysical Flows*. Academic Press, New York.
- Keulegan, G.H., 1958. The motion of saline fronts in still water. Technical Report 339, US Nat. Bur. Stand.
- Kunze, E., Sanford, T., 1996. Abyssal mixing: where it is not. *J. Phys. Oceanogr.* 26, 2286–2296.
- Kunze, E., Toole, J., 1997. Tidally driven vorticity, diurnal shear, and turbulence atop fieberling seamount. *J. Phys. Oceanogr.* 27, 2663–2693.
- Lam, C., Bremhorst, K., 1981. Modified form of the k - ϵ model for predicting wall turbulence. *J. Fluids Eng.* 103 (3), 456–460.
- Lavelle, J., Lozovatsky, I., Smith, D., 2004. Tidally induced turbulent mixing at Irving seamount – modeling and measurements. *Geophys. Res. Lett.* 31 (L10308). doi:10.1029/2004GL019706.
- Ledwell, J., Montgomery, E., Polzin, K., St. Laurent, R.S.L.C., Toole, J., 2000. Evidence for enhanced mixing over rough topography in the abyssal ocean. *Nature* 403, 179–182.
- Lilly, D., 1967. The representation of small scale turbulence in numerical simulation experiments. In: Goldstine, H. (Ed.), *Proc. IBM Sci. Computing Symp. On Environmental Sciences*, Yorktown Heights, NY, pp. 195–210.
- Long, R.R., 1972. The steepening of long, internal waves. *Tellus* 24, 88–99.
- Lueck, R., Mudge, T., 1997. Topographically induced mixing around a shallow seamount. *Science* 276, 1831–1833.
- Maday, Y., Patera, A.T., 1989. Spectral element methods for the Navier–Stokes equations. In: Noor, A.K. (Ed.), *State of the Art Surveys in Computational Mechanics*. ASME, pp. 71–143.
- Maday, Y., Patera, A.T., Ronquist, E.M., 1990. An operator-integration-factor splitting method for time-dependent problems: application to incompressible fluid flow. *J. Sci. Comput.* 10, 496–508.
- Marsden, A., Vasilyev, O., Moin, P., 2002. Construction of commutative filters for LES on unstructured meshes. *J. Comput. Phys.* 175, 584–603.
- Meneveau, C., Lund, T., Cabot, W., 1996. A Lagrangian dynamic subgrid-scale model of turbulence. *J. Fluid Mech.* 319, 353–385.
- Métais, O., 1998. Large-eddy simulations of three-dimensional turbulent flows: geophysical applications. In: Chassignet, E.P., Vernon, J. (Eds.), *Ocean Modeling and Parameterization, NATO Science Series, Series C: Mathematical and Physical Sciences*, vol. 516. Kluwer Academic Publishers, Dordrecht, The Netherlands, pp. 351–372.
- Miles, J.W., 1961. On the stability of heterogeneous shear flows. *J. Fluid Mech.* 10, 496–508.
- Moin, P., Kirn, J., 1982. Numerical investigation of turbulent channel flow. *J. Fluid Mech.* 117, 341–377.
- Moum, J., 1996. Energy containing scales of turbulence in the ocean thermocline. *J. Geophys. Res. Oceans* 101 (C6), 14085–14109.
- Munk, W., Wunsch, C., 1998. Abyssal recipes II: energetics of tidal and wind mixing. *Deep Sea Res. I* 45, 1977–2010.
- Nabatov, V., Ozmidov, R., 1988. A study of turbulence over underwater mountains in the Atlantic ocean (in Russian). *Oceanology* 28, 210–217.
- Özgökmen, P.F.T.M., Johns, W., 2006. Product water mass formation by turbulent density currents from a high-order nonhydrostatic spectral element model. *Ocean Modell.* 12, 237–267.
- Özgökmen, T.M., Fischer, P.F., Duan, J., Iliescu, T., 2004a. Three-dimensional turbulent bottom density currents from a high-order nonhydrostatic spectral element model. *J. Phys. Oceanogr.* 34 (9), 2006–2026.
- Özgökmen, T.M., Fischer, P.F., Duan, J., Iliescu, T., 2004b. Entrainment in bottom gravity currents over complex topography from three-dimensional nonhydrostatic simulations. *Geophys. Res. Lett.* 31 (L13212). doi:10.1029/2004GL020186.
- Pacanowski, R.C., Philander, S., 1981. Parameterization of vertical mixing in numerical models of tropical oceans. *J. Phys. Oceanogr.* 11, 1443–1451.
- Patera, A., 1984. A spectral element method for fluid dynamics; laminar flow in a channel expansion. *J. Comput. Phys.* 54, 468–488.
- Pawlak, G., MacCready, P., Edwards, K.A., McCabe, R., 2003. Observations on the evolution of tidal vorticity at a stratified deep water headland. *Geophys. Res. Lett.* 30. doi:10.1029/2001JC001234.
- Peters, H., Gregg, M.C., Toole, J.M., 1989. On the parameterization of equatorial turbulence. *J. Geophys. Res.* 93, 1199–1218.
- Piomelli, U., Balaras, E., 2002. Wall-layer models for large-eddy simulations. *Ann. Rev., Fluid Mech.* 34, 349–374.
- Pope, S., 2000. *Turbulent Flows*. Cambridge University Press, Cambridge, ISBN 0-521-59886-9.
- Porte-Agel, F., Meneveau, C., Parlange, M.B., 2000. A scale-dependent dynamic model for large-eddy simulation: application to a neutral atmospheric boundary layer. *J. Fluid Mech.*, 0022-1120 415, 261–284.
- Price, J.F., Baringer, M.O., 1994. Outflows and deep water production by marginal seas. *Prog. Oceanogr.* 33, 161–200.
- Raasch, S., Etling, D., 1998. Modeling deep ocean convection: large eddy simulation in comparison with laboratory experiment. *J. Phys. Oceanogr.* 28, 1786–1802.

- Reynolds, W.C., 1989. The potential and limitations of direct and large eddy simulations. In: Lumley, J.L. (Ed.), *Wither Turbulence? Turbulence at the Crossroads, Lecture Notes on Physics*, vol. 357. Springer-Verlag, pp. 313–343.
- Riley, J.J., Lelong, M.-P., 2000. Fluid motions in the presence of strong stable stratification. In: *Annual Reviews, Palo Alto, CA, 2000. Annual Review of Fluid Mechanics*, vol. 32, pp. 613–657.
- Rohr, J.J., Itsweire, E.C., Helland, K.N., Atta, C.W.V., 1988. Growth and decay of turbulence in stably stratified shear flow. *J. Fluid Mech.* 195, 77–111.
- Safman, P., Wilcox, D., 1974. Turbulence modeling predictions for turbulent boundary layers. *AIAA J.* 12, 541.
- Sagaut, P., 2005. *Large eddy simulation for incompressible flows*, Scientific Computation, Springer-Verlag, Berlin, An introduction, third ed. ISBN 3-540-67890-5.
- Schmidt, H., Schumann, U., 1989. Coherent structure of the convective boundary layer derived from large-eddy simulations. *J. Fluid Mech.* 200, 511–562.
- Schumann, U., 1975. Subgrid scale model of finite difference simulations of turbulent flows in plane channels and annuli. *J. Comput. Phys.* 18, 376–404.
- Schumann, U., 1991. Subgrid length-scales for large-eddy simulation of stratified turbulence. *Theor. Comput. Fluid Dyn.* 2, 279–290.
- Scotti, A., Piomelli, U., 2002. Turbulence models in pulsating flows. *AIAA J.* 40 (3), 537–544.
- Siegel, D.A., Domaradzki, J.A., 1994. Large-eddy simulation of decaying stably stratified turbulence. *J. Phys. Oceanogr.* 24, 2353–2386.
- Simpson, J.E., 1987. *Gravity Currents in the Environment and the Laboratory*. John Wiley and Sons, New York.
- Skyllingstad, E., Wijesekera, H., 2004. Large-eddy simulation of flow over two-dimensional obstacles: high drag states and mixing. *J. Phys. Oceanogr.* 34, 94–112.
- Skyllingstad, E., Smyth, W., Moum, J., Wijesekera, H., 1999. Upper-ocean turbulence during a westerly wind burst: a comparison of large-eddy simulation results and microstructure measurements. *J. Phys. Oceanogr.* 20, 5–28.
- Smagorinsky, J., 1963. General circulation experiments with the primitive equations. *Mon. Weather Rev.* 91, 99–164.
- Spalart, P.R., Almaras, S.R., 1994. A one-equation turbulence model for aerodynamic flows. *La Rech. Aerospaciale* 1 (1), 5–21.
- Stanley, L., Stewart, D., 2002. *Design Sensitivity Analysis, Frontiers in Applied Mathematics*, vol. 25. Society for Industrial and Applied Mathematics (SIAM), Philadelphia, PA, ISBN 0-89871-524-5. Computational issues of sensitivity equation methods.
- Stevens, B., Moeng, C.-H., Sullivan, P.P., 1998. Entrainment and subgrid lengthscales in large-eddy simulations of atmospheric boundary layer flows. In: Kerr, R.M., Kimura, Y. (Eds.), *Developments in Geophysical Turbulence*. Kluwer, pp. 253–269.
- Stevens, B., Moeng, C.-H., Sullivan, P.P., 1999. Large-eddy simulations of radiatively driven convection: sensitivities to the representation of small scales. *J. Atmos. Sci.* 56 (23), 3963–3984.
- Strang, E.J., Fernando, H.J.S., 2001. Entrainment and mixing in stratified shear flows. *J. Fluid Mech.* 428, 349–386.
- Taylor, G., 1935. Statistical theory of turbulence. *Proc. Roy. Soc. London A* 151, 421–454.
- Thorpe, S.A., 1977. Turbulence and mixing in a Scottish loch. *Philos. Trans. Roy. Soc. London A* 286, 125–181.
- Thurnherr, A., Speer, K., 2003. Boundary mixing and topographic blocking on the mid-Atlantic ridge in the south Atlantic. *J. Phys. Oceanogr.* 33, 848–862.
- Tufo, H.M., Fischer, P., 2001. Fast parallel direct solvers for coarse grid problems. *J. Parallel Distr. Comput.* 173, 431–471.
- van der Bos, F., Geurts, B.J., 2005. Commutator-errors in the filtering approach to large-eddy simulation. *Phys. Fluids*. 17 (3). Art. No. 035108.
- Vasilyev, O., Lund, T., Moin, P., 1998. A general class of commutative filters for LES in complex geometries. *J. Comput. Phys.*, 0021-9991 146 (1), 82–104.
- Wang, D., McWilliams, J., Large, W., 1996. Large-eddy simulation of the equatorial ocean boundary layer: diurnal cycling, eddy viscosity, and horizontal rotation. *J. Geophys. Res.* 101 (C2), 3649–3662.
- Wang, D., McWilliams, J., Large, W., 1998. Large-eddy simulation of the diurnal cycle of deep equatorial turbulence. *J. Phys. Oceanogr.* 28, 129–148.
- Wilcox, D., 1998. *Turbulence Modeling for CFD*, second ed. DCW Industries, Inc.
- Winters, K.B., Lombard, P.N., Riley, J.J., D’Asaro, E.A., 1995. Available potential energy and mixing in density-stratified fluids. *J. Fluid Mech.* 289, 115–128.